Active and Passive Microwave, and LIDAR Remote Sensing

9

Passive remote sensing systems record electromagnetic energy that was reflected (e.g., blue, green, red, and near-infrared light) or emitted (e.g., thermal infrared energy) from the surface of the Earth. There are also *active* remote sensing systems that are not dependent on the Sun's electromagnetic energy or the thermal properties of the Earth. Active remote sensors create their own electromagnetic energy that 1) is transmitted from the sensor toward the terrain (and is largely unaffected by the atmosphere), 2) interacts with the terrain producing a backscatter of energy, and 3) is recorded by the remote sensor's receiver. The most widely used active remote sensing systems include:

- *active microwave* (*RADAR*), which is based on the transmission of long-wavelength microwaves (e.g., 3 – 25 cm) through the atmosphere and then recording the amount of energy backscattered from the terrain;

- *LIDAR*, which is based on the transmission of relatively short-wavelength laser light (e.g., 0.90 μm) and then recording the amount of light backscattered from the terrain; and

- *SONAR*, which is based on the transmission of sound waves through a water column and then recording the amount of energy backscattered from the bottom or from objects within the water column.

Of the three, RADAR remote sensing is the most widely used for Earth resource observations, although SONAR and LIDAR are quite useful for specific applications (e.g., bathymetric mapping and measurement of terrain elevation, respectively). It is also possible to record passive microwave energy that is naturally emitted from the surface of the Earth using a *passive microwave radiometer*. This chapter includes an overview of passive microwave remote sensing as well as the fundamental principles of LIDAR.

History of Active Microwave (RADAR) Remote Sensing

James Clerk Maxwell (1831– 1879) provided the fundamental mathematical descriptions of the magnetic and electric fields associated with electromagnetic radiation. Then, Heinrich R. Hertz (1857 – 1894) increased our knowledge about the creation and propagation of electromagnetic energy in the microwave and radio portions of the spectrum. Hertz also studied the interaction of radio waves with metallic surfaces and thus initiated some of the early

thinking that would eventually lead to radios and radars. Building on the fundamental physics principles discovered by Maxwell and Hertz, Guglielmo M. Marconi (1874 – 1937) constructed an antenna that transmitted and received radio signals. In 1901, he sent radio waves across the Atlantic and in 1909 shared the Nobel prize in physics for his work.

RADAR as we know it was investigated by A. H. Taylor and L. C. Young in 1922. These scientists positioned a high-frequency radio transmitter on one side of the Anacostia River near Washington, DC and a receiver on the opposite side. Ships passing up or down the river interrupted the very long wavelength radio signal (1 – 10 m) sent between the transmitter and receiver. Such systems provided the first clues that radio signals might be useful for detecting the distance to ships (i.e., the range) at sea. This had implications for ship navigation because the active radio transmission and reception could take place both at night and even in bad weather (Campbell, 1996). The military took an early interest in radar because in times of war it is important to know the location of all ships and planes (friendly and enemy) at all times. A phrase describing the process was "**ra**dio **d**etection **a**nd **r**anging" or *RADAR*. Although radar systems now use microwave wavelength energy almost exclusively instead of radiowaves, the acronym was never changed.

By 1935 Young and Taylor (and independently Sir Robert Watson-Watt in Great Britain) combined the antenna transmitter and receiver in the same instrument. Eventually, high-power transmissions in very specific bands of the electromagnetic spectrum were possible. These and other electronic advancements laid the groundwork for the development of RADAR during World War II for navigation and target location. By late 1936 experimental radars were working in the United States, Great Britain, Germany, and the Soviet Union. Of these nations, none was more vulnerable to air attack than Britain. London lay within 90 miles of foreign territory and within 275 miles of Germany. Under the direction of Air Chief Marshal Hugh Dowding, the British constructed 21 radars along the south and east coasts of England and the east coast of Scotland. The code name "Chain Home — CH" arose from a plan to build a "home chain" of radars in Britain to be followed by an overseas chain to defend threatened portions of the British empire. The CH radars were the primary British long-range early warning radars until well into World War II. The radars allowed incoming planes to be detected out to a maximum range of 50 miles. Without the radar, Britain would not have been able to effectively counter the German Luftwaffe bombers and fighter escorts especially during the Battle of Britain, which began in July 1940 (Fisher, 1988; Price, 1990). The circularly scanning Doppler radar that we watch every day during television weather updates to identify the geographic location of storms around cities is based on the same circularly scanning radar concept (plan-position indicator radar, PPI) found in the original World War II radars. PPI radars are also used for air-traffic control at airports.

RADAR images obtained from aircraft or spacecraft as we know them today were not available during World War II. The continuous-strip mapping capability of *side-looking airborne radar (SLAR)* was not developed until the 1950s. An important advantage of SLAR is its ability to obtain reconnaissance images over vast regions to the left or right of the aircraft (Sabins, 1997). This is called *long-range standoff* because the pilot can fly at the edge of friendly air-space while obtaining detailed RADAR imagery far into potentially unfriendly air space (Avery and Berlin, 1992). It also became possible to perform *radargrammetric* measurement — the science of extracting quantitative geometric object information from radar images (Leberl, 1990; Henderson and Lewis, 1998).

The military began using SLARs in the 1950s. By the mid-1960s some systems were declassified. There are two primary types of SLAR: *real aperture radar* (also known as brute-force radar) and *synthetic aperture radar (SAR)*, where the word "aperture" means *antenna*. Real aperture radars use an antenna of fixed length, e.g., 1 – 2 m. Synthetic aperture radars also use a 1 – 2 m antenna, but they are able to synthesize a much larger antenna (e.g., perhaps 600 m in length), which has improved resolving power. SARs achieve very fine resolution from great distances. For example, an 11-m SAR antenna on an orbital platform can be synthesized electronically to have a synthetic length of 15 km. Later it will be demonstrated how important this capability is to SAR azimuth resolution. Most military and civilian commercial RADARS are now synthetic aperture radars.

In the 1960s and 1970s, both real aperture and synthetic aperture SLARs were used extensively for rapid Earth resource reconnaissance mapping of vast, previously unmapped regions of the continents. Early studies focused on continents perennially shrouded in cloud cover. The first large-scale project for mapping terrain with side-looking airborne radar was a complete survey of the province of Darien, which connects Panama and South America. In 1968, Westinghouse Electric, Inc., in cooperation with Raytheon, Inc., employed a real aperture SLAR that Westinghouse developed for the U.S. Army and successfully made a 20,000 km^2 mosaic of this area (Jensen et al., 1977). Up to this time, the area had never been seen or mapped in its entirety because of almost perpetual cloud cover.

Table 9-1. Characteristics of Selected Earth Orbiting Synthetic Aperture Radars (SAR)

Parameter	SEASAT	SIR-A	SIR-B	SIR-C/X-SAR	ALMAZ-1	ERS-1,2	JERS-1	RADARSAT
Launch date	June 26, 1978	November 12, 1981	October 5, 1984	April 1994 October 1994	March 31, 1991	1991 1995	February 11,1992	November 1995
Nationality	USA	USA	USA	USA	Soviet Union	Europe	Japan	Canada
Wavelength, cm	L - (23.5)	L - (23.5)	L - (23.5)	X - (3.0) C - (5.8) L - (23.5)	S - (9.6)	C - (5.6)	L - (23.5)	C - (5.6)
Depression angle, ° (near to far-range) [incident angle]	73 – 67° [23°]	43 – 37° [50°]	75 – 35° [15 – 64°]	variable [15 – 55°]	59 – 40° [30 – 60°]	67° [23°]	51° [39°]	70 – 30° [10° – 60°]
Polarization	HH	HH	HH	HH, HV, VV,VH	HH	VV	HH	HH
Azimuth resolution, m	25	40	17 – 58	30	15	30	18	8 – 100
Range resolution, m	25	40	25	10 – 30	15 – 30	26	18	8 – 100
Swath width, km	100	50	10 – 60	15 – 90	20 – 45	100	75	50 – 500
Altitude, km	800	260	225 and 350	225	300	785	568	798
Latitude coverage, °	10° - 75° N	41° N - 36° S	60° N - 60° S	57° N - 57° S	73° N - 73° S	near-polar orbit	near-polar orbit	near-polar orbit
Mission duration	105 days	2.5 days	8 days	10 days	18 months	--	6.5 years	--

Goodyear Aerospace, Inc., and the Aero Service Division of Western Geophysical, Inc., adapted a synthetic aperture radar built by Goodyear and installed it in an Aero Service Caravelle jet for civilian surveys. In 1971 they initiated project RADAM (Radar of the Amazon) to map the Amazon Basin in Venezuela and Brazil. Approximately 4 million km^2 of land area (about half the size of the United States) were recorded and assembled into radar mosaics. Goodyear and Aero Service eventually surveyed the Amazon rain forest in Brazil, Venezuela, eastern Colombia, Peru, and Bolivia. Subsequent radar investigations mapped Guatemala, Nigeria, and Togo, and portions of Indonesia, the Philippines, Peru, and other regions that were previously unmapped (Leberl, 1990).

NASA has launched two successful SARs, SEASAT and the ongoing Space Shuttle Imaging Radar experiments. *SEASAT* (for "sea satellite") was launched in 1978 to obtain L-band (23.5 cm) 25 x 25 m spatial resolution oceanographic information (Table 9-1). This was the first orbital SAR that provided public-domain data. It also provided valuable land information, but functioned for only 105 days. The *Shuttle Imaging Radar* experiment A *(SIR-A)* with its L-band (23.5 cm) 40 x 40 m SAR was launched in 1981, SIR-B was launched in 1984 with its 17 x 25 m resolution, and SIR-C in 1994 with its multifrequency and multipolarization capability. SIR-A, SIR-B, and SIR-C missions lasted only 2.5, 8, and 10 days, respectively.

The former Soviet Union launched the ALMAZ-1 S-band (9.6 cm) radar in 1991. The European Space Agency (ESA) launched their *European Remote Sensing Satellite ERS-1* with its C-band (5.6 cm) imaging radar in 1991 and *ERS-2* in 1995. Japan launched the L-band (23.5 cm) *Japanese Earth Resources Satellite JERS-1* in 1992. The Canadian government placed the C-band (5.6 cm) *RADARSAT-1* in orbit in 1995. RADARSAT-2 is scheduled for launch early in the twenty-first century. The system characteristics of these orbital SAR systems are summarized in Table 9-1 and will be discussed later in this chapter.

Active and passive microwave remote sensing will continue to be very important research areas in the coming decades. Such sensors provide the only viable information for the tropical portions of the world where extensive, fragile ecosystems are at risk and under perennial cloud cover. For a

a. Intermap LearJet 36 Star 3*i*

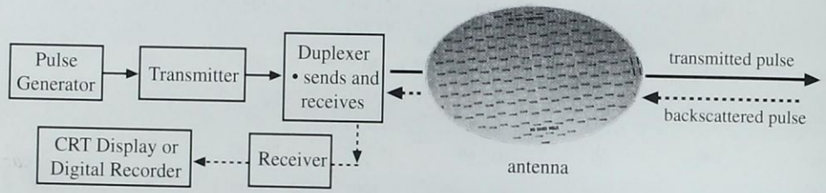

b. Typical active microwave system components

Figure 9-1 a) A side-looking airborne radar (SLAR) called the Star 3*i* IFSAR (interferometric synthetic aperture radar) is mounted underneath a LearJet 36 aircraft (courtesy Intermap Technologies, Inc.). b) The active microwave system components and flow of energy through a typical SLAR. It consists of a pulse-generating device, transmitter, duplexer, antenna, receiver, and a digital recorder. Some systems have a quick-look CRT display to make sure data is being collected. The 1-m synthetic aperture antenna shown can synthesize an antenna hundreds of meters long.

more detailed history of radar development, see Leberl (1990) and Henderson and Lewis (1998). The primary and secondary advantages of RADAR remote sensing are summarized in Table 9-2.

Active Microwave System Components

Active microwave imagery is obtained using instruments and principles that are different from those used when acquiring data in the visible, near-, mid-, and thermal infrared portions of the spectrum using passive remote sensing techniques. Therefore, it is necessary to understand the active microwave system components and how electromagnetic energy is sent, received, and recorded by the sensor system before an analyst can accurately interpret a radar image. The discussion is based initially on the system components and functions of a *real aperture side-looking airborne radar* (SLAR). The discussion then expands to include *synthetic aperture radars* (SAR) that have improved capabilities.

Sending and Receiving a Pulse of Microwave Electromagnetic Energy - System Components

A typical active microwave SLAR is shown mounted on an aircraft in Figure 9-1a. It consists of a pulse-generating device, a transmitter, a duplexer that carefully coordinates when the active microwave energy is transmitted and received, an antenna, a receiver, a recording device such as a high-density digital tape recorder or hard disk, and typically a CRT monitor so that the technician in the plane can make sure radar imagery is actually being collected (Figure 9-1b). The radar can also be mounted onboard a satellite. The pulse-generating device sends a pulse of electromagnetic energy at a specific wavelength (frequency) to the transmitter. When in sending mode, the duplexer then sends the polarized pulse of energy through the antenna toward the Earth's surface.

Table 9-2. Advantages of RADAR Remote Sensing of the Environment (after Leberl, 1990)

Advantages
Primary
• Active microwave energy penetrates clouds and serves as an all-weather remote sensing system.
• Synoptic views of large areas, for mapping at 1:25,000 to 1:400,000. Satellite coverage of entire cloud-shrouded countries is possible.
• Coverage can be obtained at user-specified times, even at night.
• Permits imaging at shallow look angles, resulting in different perspectives that cannot always be obtained using aerial photography.
• Senses in wavelengths outside the visible and infrared regions of the electromagnetic spectrum, providing information on surface roughness, dielectric properties, and moisture content.
Secondary
• May penetrate vegetation, sand, and surface layers of snow.
• Has its own illumination, and the angle of illumination can be controlled.
• Enables resolution to be independent of distance to the object, with the size of a resolution cell being as small as 1 x 1 m.
• Images can be produced from different types of polarized energy (HH, HV, VV, VH).
• May operate simultaneously in several wavelengths (frequencies) and thus has multifrequency potential.
• Can measure ocean wave properties, even from orbital altitudes.
• Can produce overlapping images suitable for stereoscopic viewing and radargrammetry.
• Supports interferometric operation using two antennas for 3-D mapping, and analysis of incident-angle signatures of objects.

Wavelength, Frequency and Pulse Length

The pulse of electromagnetic radiation sent out by the transmitter through the antenna is of a specific wavelength and duration (i.e., it has a *pulse length* measured in microseconds, μsec). The wavelengths of energy most commonly used in imaging radars are summarized in Table 9-3. The wavelengths are much longer than visible, near-infrared, mid-infrared, or thermal infrared energy used in other remote sensing systems (Figure 9-2). Therefore, microwave energy is usually measured in centimeters rather than micrometers (Carver, 1988). The unusual names associated with the radar wavelengths (e.g., K, K_a, K_u, X, C, S, L, and P) are an artifact of the original secret work on radar remote sensing when it was customary to use the alphabetic descriptor instead of the actual wavelength or frequency. These descriptors are still used today in much of the radar scientific literature. SIR-C and the NASA Jet Propulsion Lab suborbital AIRSAR radar operate in more than one frequency. These systems produce *multifrequency radar* imagery.

Table 9-3. RADAR Wavelengths and Frequencies Used in Active Microwave Remote Sensing Investigations

RADAR Band Designations (common wavelengths shown in parentheses)	Wavelength (λ) in cm	Frequency (υ) in GHz
K_a (0.86 cm)	0.75 – 1.18	40.0 – 26.5
K	1.19 – 1.67	26.5 – 18.0
K_u	1.67 – 2.4	18.0 – 12.5
X (3.0 and 3.2 cm)	2.4 – 3.8	12.5 – 8.0
C (7.5, 6.0 cm)	3.9 – 7.5	8.0 – 4.0
S (8.0, 9.6, 12.6 cm)	7.5 – 15.0	4.0 – 2.0
L (23.5, 24.0, 25.0 cm)	15.0 – 30.0	2.0 – 1.0
P (68.0 cm)	30.0 – 100	1.0 – 0.3

Table 9-3 and Figure 9-2 also provide the radar band designation in units of frequency measured in billions of cycles per second (Gigahertz or GHz, 10^9 cycles sec^{-1}). Earth resource image analysts seem to grasp the concept of wavelength more readily than frequency, so the convention is to describe a radar in terms of its wavelength. Conversely, engineers generally prefer to work in units of frequency because as radiation passes through materials of different densities, frequency remains constant while velocity and wavelength change. Since wavelength (λ) and frequency (υ) are inversely related to the speed of light (c), it really does not matter which unit of measurement is used as long as one remembers the following relationships:

$$c = \lambda\upsilon \tag{9-1}$$

$$\lambda = \frac{3 \times 10^8 \text{ m sec}^{-1}}{\upsilon} \tag{9-2}$$

$$\upsilon = \frac{3 \times 10^8 \text{ m sec}^{-1}}{\lambda}. \tag{9-3}$$

The following simple equation can be used to rapidly convert frequencies into units of radar wavelength:

$$\lambda \text{ in centimeters} = \frac{30}{\upsilon \text{ (in GHz)}}. \tag{9-4}$$

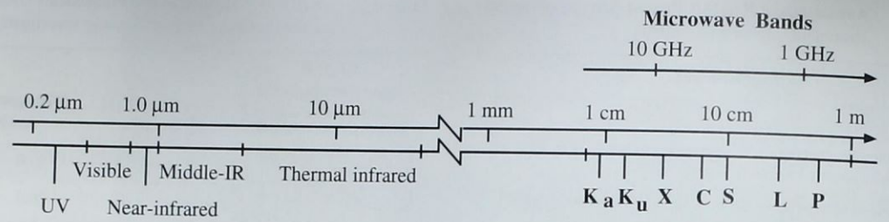

Figure 9-2 The wavelength and frequency of commonly used RADAR bands. RADAR antennas transmit and receive very long wavelength energy measured in centimeters, unlike the relatively short wavelength visible, near-infrared, middle-infrared, and thermal infrared regions measured in micrometers (after Carver, 1988).

Azimuth and Range Direction, Depression Angle, Incident Angle, and Polarization

There are additional parameters that must be known about the nature of the pulse of microwave energy that is sent by the radar antenna to the terrain, including aircraft *azimuth direction*, *radar range* or *look direction, depression angle, incident angle,* and *polarization.* The following discussion is based on the use of an airborne radar system, although the principles are equally applicable to satellite radar systems.

Azimuth Direction: In a typical SLAR configuration the antenna is mounted beneath and parallel to the aircraft fuselage (Figure 9-3). The aircraft travels in a straight line that is called the *azimuth flight direction*. Pulses of active microwave electromagnetic energy illuminate strips of the terrain at right angles (orthogonal) to the aircraft's direction of travel, which is called the *range* or *look direction*. Figure 9-3 depicts an aircraft equipped with a SLAR system that is illuminating the terrain on one side of the aircraft but not beneath it. The pulses of energy sent out in the range direction only illuminate a certain part of the terrain. The terrain illuminated nearest the aircraft in the line of sight is called the *near-range* (Figure 9-3). The farthest point of terrain illuminated by the pulse of energy is called the *far-range*.

Range Direction: The *range* or *look direction* for any *radar* image is the direction of the radar illumination that is at right angles to the direction the aircraft or spacecraft is traveling. Look direction usually has a significant impact on feature interpretation. The extent to which linear features are enhanced or suppressed on the imagery depends significantly on their orientation relative to a given look direction of radar illumination. Generally, objects that trend (or strike) in a direction that is orthogonal (perpendicular) to the range or look direction are enhanced much more than those objects in the terrain that lie parallel to the look direction. Consequently, linear features that appear dark or are imperceptible in a radar image using one look direction may appear bright in another radar image with a different look direction. A good example of this is demonstrated in Figure 9-4 which shows radar imagery of an area in Nigeria, West Africa, that were obtained using two different look directions. Note how certain terrain features are emphasized and/or deemphasized in the two images.

Depression Angle: The *depression angle* (γ) is the angle between a horizontal plane extending out from the aircraft fuselage and the electromagnetic pulse of energy from the antenna to a specific point on the ground (Figure 9-3). The depression angle within a strip of illuminated terrain varies from the *near-range depression angle* to the *far-range depression angle*. The *average depression angle* of a radar image is computed by selecting a point midway between the near and far-range in the image strip. Summaries of radar systems often only report the average depression angle.

Incident Angle: The *incident angle* (θ) is the angle between the radar pulse of electromagnetic energy and a line perpendicular to the Earth's surface where it makes contact. When the terrain is flat, the incident angle (θ) is the complement ($\theta = 90 - \gamma$) of the depression angle (γ). However, if the terrain is sloped, there is no relationship between depression angle and incident angle. The incident angle best describes the relationship between the radar beam and surface slope. A schematic diagram of the relationship is shown in Figure 9-5. Many mathematical radar studies assume the terrain surface is flat (horizontal) therefore, the incident angle is assumed to be the complement of the depression angle.

Polarization: Unpolarized energy vibrates in *all* possible directions perpendicular to the direction of travel. Radar antennas send and receive *polarized* energy. This means that the pulse of energy is filtered so that its electrical wave vibrations are only in a single plane that is perpendicular to the direction of travel. The pulse of electromagnetic energy

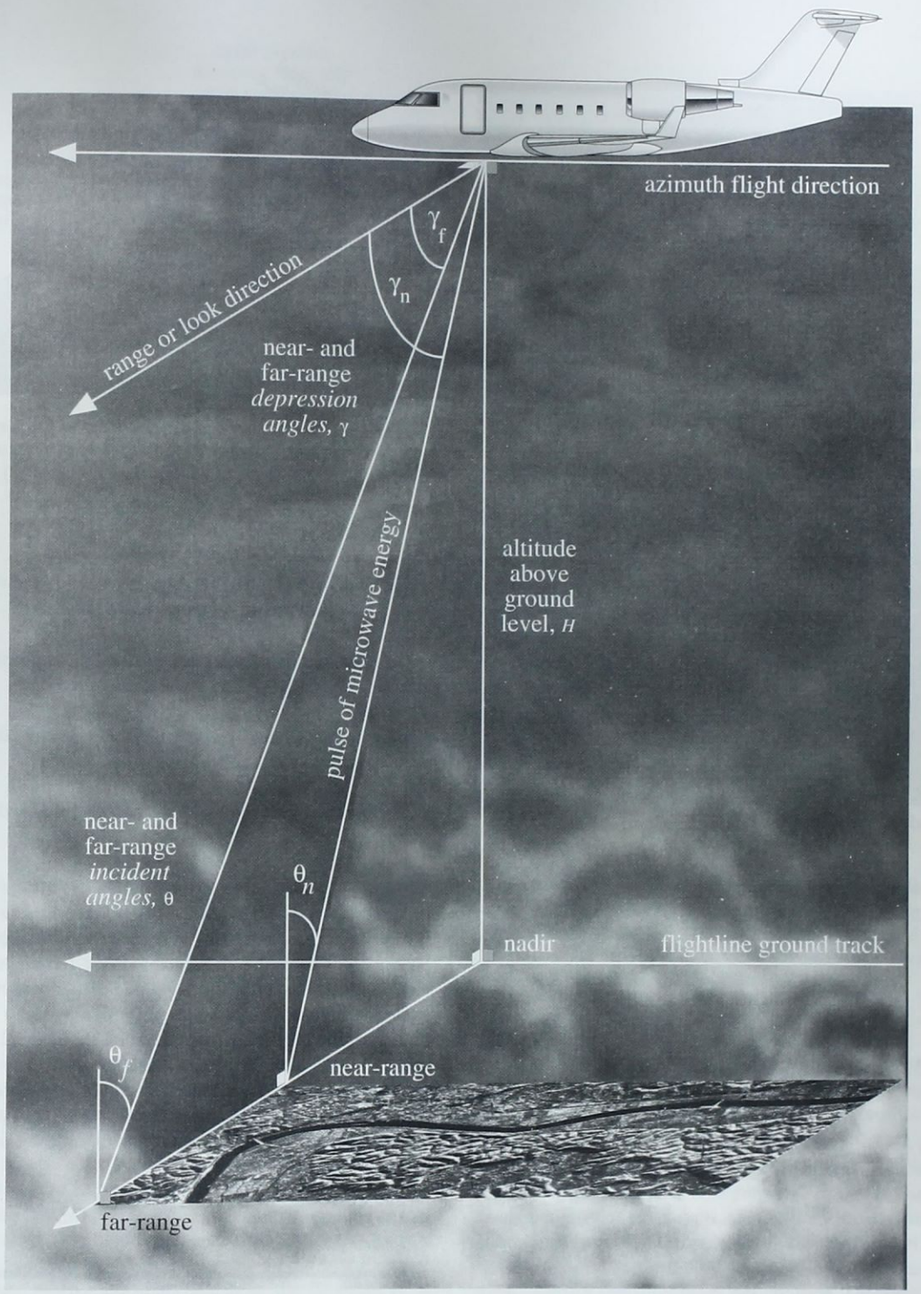

Figure 9-3 Geometric characteristics of radar imagery acquired by a side-looking airborne radar (SLAR) through cloud cover. All the nomenclature assumes that the terrain is flat.

a.
X-band, HH polarization ↑ look direction

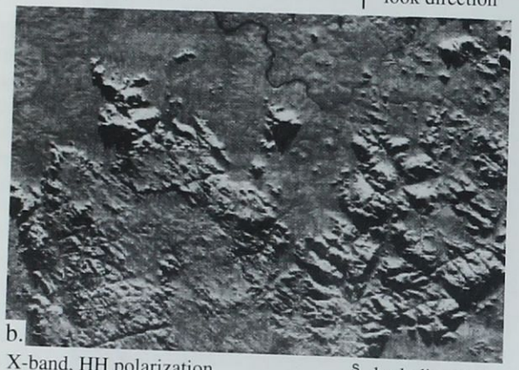

b.
X-band, HH polarization ↓ look direction (S)

Figure 9-4 a) X-band image of the Kaduna State in Nigeria created by flying east-west and having the RADAR look north. b) This image was obtained by flying the aircraft east-west with the RADAR looking south. Generally, it is good practice to always orient a radar image so that the look direction is toward the viewer. This causes the shadows to fall toward the analyst and keeps him or her from experiencing pseudoscopic illusion (i.e., topographic inversion).

sent out by the antenna may be *vertically* or *horizontally polarized* as shown in Figure 9-6. The transmitted pulse of electromagnetic energy interacts with the terrain and some of it is backscattered at the speed of light toward the aircraft or spacecraft where it once again must pass through a filter. If the antenna accepts the backscattered energy, it is recorded. Various types of backscattered polarized energy may be recorded by the radar. For example, it is possible to:

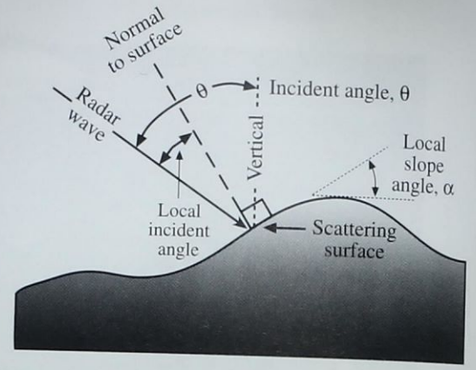

Figure 9-5 The relationship between radar incident angle (θ), true vertical, and local slope angle (α) for non-level terrain (after Henderson and Lewis, 1998).

- send vertically polarized energy and receive only vertically polarized energy (designated *VV*),
- send horizontal and receive horizontally polarized energy (*HH*),
- send horizontal and receive vertically polarized energy (*HV*), or
- send vertical and receive horizontally polarized energy (*VH*).

HH and *VV* configurations produce *like-polarized* radar imagery. *HV* and *VH* configurations produce *cross-polarized* imagery. The ability to record different types of polarized energy from a resolution element in the terrain results in valuable Earth resource information in certain instances. For example, Figure 9-7 demonstrates how a northern Arizona basalt lava flow is much easier to delineate in the HH polarization real aperture K_a-band radar image than in the HV polarization image acquired at the same time. More will be said about how the terrain interacts with a pulse of polarized electromagnetic energy in the section on radar environmental considerations.

Slant-Range versus Ground-Range RADAR Image Geometry

Radar imagery has a different geometry than that produced by most conventional remote sensor systems, such as cameras, multispectral scanners or area-array detectors. Therefore, one must be very careful when attempting to make radargrammetric measurements. First, uncorrected radar imagery is displayed in what is called *slant-range geometry*, i.e., it is based on the actual distance from the radar to each of the respective features in the scene. For example, in Figure 9-8 we see two fields, A and B, that are the same size in the real world. One field is in the near-range close to the aircraft and one is in the far-range. Field A in the near-range is compressed much more than field B in the far-range in a slant-range display (Ford et al., 1980). It is possible to convert the *slant-range display* (S_{rd}) information into the true *ground-range display* (G_{rd}) on the x-axis so that features in the scene are in their proper planimetric (x,y) position relative to one another in the final radar image. The following equation, based on the Pythagorean theorem applied to a right triangle, transforms the slant-range distance, S_{rd}, at the very beginning of field A to a corrected ground-range distance, G_{rd}, based on the trigonometric relationship between the altitude of the sensor above-ground datum (H) and the other two sides of the right triangle, S_{rd} and G_{rd}, shown in Figure 9-8:

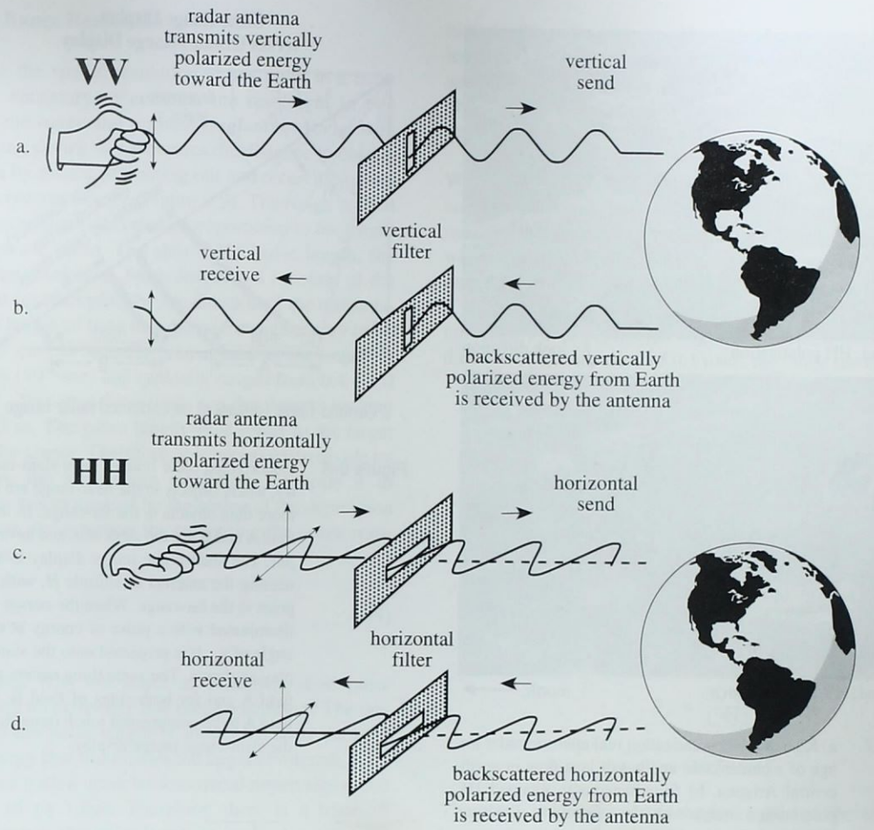

Figure 9-6 a) VV – Polarization. The radar antenna transmits vertically polarized energy toward the terrain. b) Some of the vertically polarized energy is *not* depolarized by the terrain. A vertical filter in the antenna allows only vertically polarized energy backscattered from the terrain to be recorded. c) HH – Polarization. The radar antenna transmits horizontally polarized energy toward the terrain. d) Some of the horizontally polarized energy is *not* depolarized by the terrain. A horizontal filter in the antenna allows only horizontally polarized energy backscattered from the terrain to be recorded.

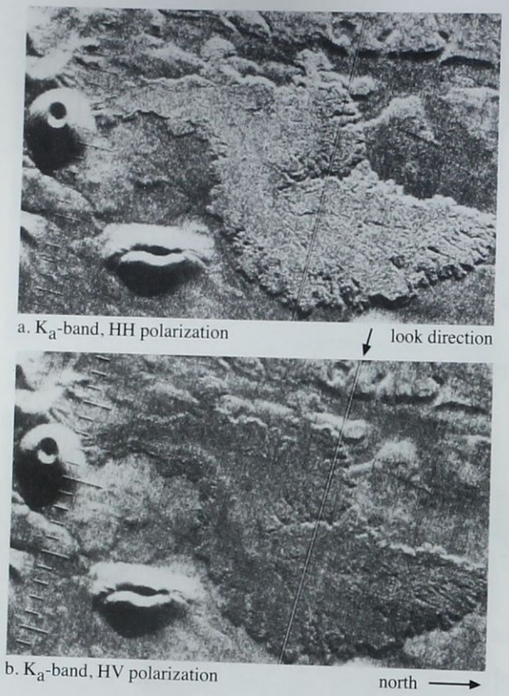

Figure 9-7 a) K_a-band, HH polarization real aperture radar image of a cinder cone and basalt lava flow in north-central Arizona. b) Simultaneously obtained HV polarization image with the same look direction. The strong response of the lava flow in the direct return image (HH) and the weak return on the cross-polarized image (HV) indicates that the blocky flow is highly polarized. This is due to the direct reflection of blocks that are large relative to the wavelength (courtesy of NASA; Carver, 1988).

$$S_{rd}^{\ 2} = H^2 + G_{rd}^{\ 2} \tag{9-5}$$

$$G_{rd} = \sqrt{S_{rd}^{\ 2} - H^2}\ . \tag{9-6}$$

It is also possible to transform the slant-range display to a ground-range display using the relationship between the height of the antenna above the local ground level, H, and the depression angle (γ) at the point of interest using the following equation (Ford et al., 1980):

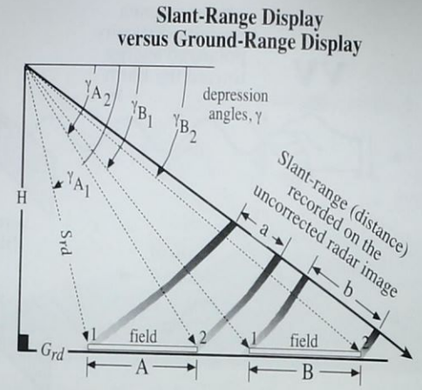

Figure 9-8 Uncorrected radar images have slant-range geometry, where objects in the near-range are compressed more than objects in the far-range. In this example, field A and B are the same size and have no local relief. The slant-range image display is a plane connecting the antenna at altitude H, with the farthest point in the far-range. When the corner of field A is illuminated with a pulse of energy at a depression angle of γ_A, it is projected onto the slant-range display as shown. The same thing occurs at the end of field A and for both sides of field B. This causes field A to be compressed much more than field B in the slant-range image display.

$$G_{rd} = H\sqrt{\frac{1}{\sin^2\gamma} - 1} \tag{9-7}$$

If we wanted to measure the true ground-range distance between two points in a radar image such as between points 1 and 2 in field A, we may use the following relationship (Henderson and Lewis, 1998):

$$G_{rd_{1-2}} = H(\cot\gamma_2 - \cot\gamma_1) \tag{9-8}$$

which takes into account the altitude of the sensor, H, and the depression angle (γ) to points 1 and 2 in the image.

These equations assume that the terrain is flat. It does not correct for distortion due to radar layover (foreshortening) caused by topographic relief (to be discussed). Radar image analysts should always inquire as to whether they are viewing radar imagery that has been converted from slant-range to ground-range geometry. Most radar systems and data providers now provide the data in ground-range geometry.

Computing Range Resolution

To determine the spatial resolution at any point in a radar image, it is necessary to compute the resolution in two dimensions: the *range* and *azimuth resolutions*. Radar is in effect a ranging device that measures the distance to objects in the terrain by means of sending out and receiving pulses of active microwave energy (Figure 9-9). The *range resolution* in the across-track direction is proportional to the length of the microwave pulse. The shorter the pulse length, the finer the range resolution. *Pulse length* is a function of the speed of light (c) multiplied by the duration of the transmission (τ). The length of time that the microwave energy (e.g., L-band, 23.5 cm) is actually transmitted is measured in microseconds (10^{-6} sec) and typically ranges from 0.4 – 1.0 microsecond. This translates into a pulse length ranging from 8 – 210 m. The pulse length must travel to the target and back to the sensor. Therefore, it is necessary to divide by 2 to measure the slant-range resolution. To scale it to ground-range, it is multiplied by the cosine of the depression angle (γ). Thus, the equation for computing the *range resolution* becomes:

$$R_r = \frac{\tau \cdot c}{2\cos\gamma}\ . \tag{9-9}$$

One might ask, Why not select an extremely short pulse length to obtain an extremely fine range resolution? The reason is that as the pulse length is shortened, so is the total amount of energy that illuminates the target of interest. Soon we would have such a weak backscattered return signal that it would be of no value. Therefore, there is a trade-off between shortening the pulse length to improve range resolution and having enough energy in the transmitted pulse to receive a strong signal from the terrain, which is the heart of microwave remote sensing.

The general rule is that signals reflected from two distinct objects in the terrain (e.g., two houses) can be resolved if their respective range distances are separated by at least half the pulse length. For example, consider Figure 9-9 in which the terrain is being illuminated with a single pulse of microwave energy that lasts 10^{-7} seconds. This translates to a pulse length of 30 m and therefore has a range resolution of 15 m. The fate of the single pulse of microwave energy is monitored for four brief time periods. At *time n* the pulse has not impacted any homes yet. At *time n+1* a portion of the pulse has been reflected back toward the antenna while the remaining part of the pulse continues across-track. By *time n+2* homes 2, 3, and 4 have reflected a part of the incident microwave energy back to the antenna. Because houses 1 and 2 were greater than 15 m apart, they will appear as distinct features in the radar imagery. However, houses 3 and 4 were less than 15 m apart; therefore, their two returns will overlap and they will be perceived by the antenna as one broad object. They will probably be difficult to resolve as individual houses in the radar image.

While the pulse length remains constant through the near- and far-range, the range resolution varies linearly from the near- to the far-range. For example, consider Figure 9-10 which depicts towers 1 and 2 that are 30 m apart in the near-range and towers 3 and 4 that are 30 m apart in the far-range. If we use Equation 9-9 to compute the range resolution in the far-range with a depression angle of 40° and a pulse length duration of transmission of 0.1 µsec, the range resolution is:

$$R_r = \frac{(0.1\times10^{-6}\,\text{sec})\cdot(3\times10^{8}\,\text{m sec}^{-1})}{2\cos 40^\circ}$$

$$R_r = \frac{\left(0.1\times\dfrac{1\ \text{sec}}{1,000,000}\right)\times\dfrac{300,000,000\ \text{m}}{\text{sec}}}{2\times0.766}$$

$$R_r = \frac{\dfrac{0.1\ \text{sec}}{1,000,000}\times\dfrac{300,000,000\ \text{m}}{\text{sec}}}{2\times0.766}$$

$$R_r = \frac{30\ \text{m}}{1.532}$$

$$R_r = 19.58\ \text{m}\,.$$

Therefore, towers 3 and 4 in the far-range must be separated by more than 19.58 m to resolve the individual towers on the radar image. Because towers 3 and 4 are separated by 30 m, it is possible to identify the individual towers. Conversely, towers 1 and 2, located at a depression angle of 65° in the near-range, would not be resolved because the range resolution in this area would be 35.5 m. The two towers would probably appear as a single bright return.

Computing Azimuth Resolution

Thus far we have only identified the length in meters of an active microwave resolution element at a specific depression angle and pulse length in the range (across-track) direction. To know both the length and width of the resolution element, we must also compute the width of the resolution element in the direction the craft is flying — the azimuth direction. *Azimuth resolution* (R_a) is determined by computing the width of the terrain strip that is illuminated by the radar beam. Real aperture active microwave radars produce a lobe-shaped beam similar to the one shown in Figure 9-11, which is nar-

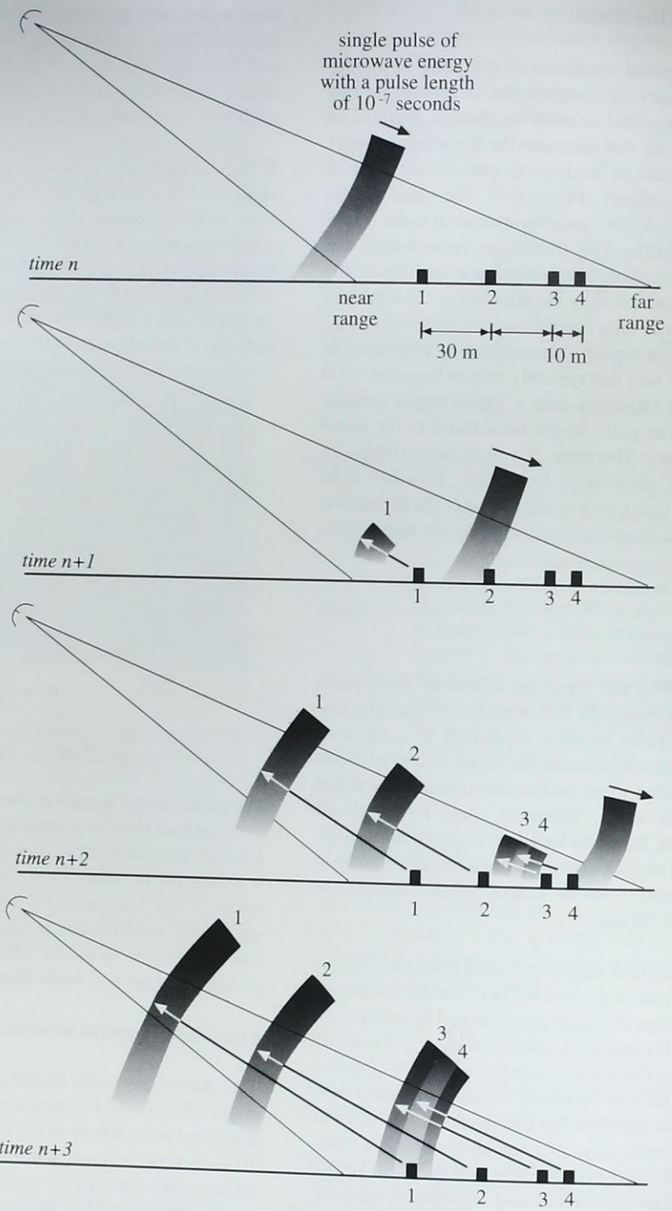

Figure 9-9 The distance of an object (its range) from the aircraft antenna is determined by the length of time required for the pulse of microwave energy traveling at the speed of light to reach the object and be reflected back to the antenna. Signals from houses 1 and 2 will arrive sooner than the signals returned from the two houses farther away (3 and 4). In this example, the 10^{-7} second pulse length equates to 30 m. The resolution across-track is equal to half the pulse length, in this case 15 m. Houses 1 and 2 will be resolved as distinct objects on the radar image. Two objects (houses 3 and 4) separated by less than half the radar pulse length will be perceived by the antenna as one broad object.

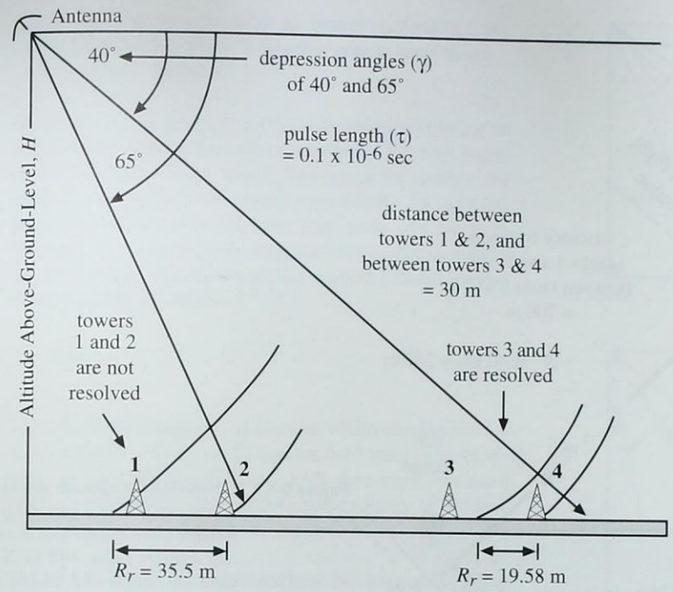

Figure 9-10 Computing the range resolution at two different depression angles (40° and 65°) for a real aperture radar with a pulse length of 0.1 x 10^{-6} sec. The towers can be resolved in the far-range but not in the near-range (after Sabins, 1997).

rower in the near-range and spreads out in the far-range. Basically, the angular beam width is directly proportional to the wavelength of the transmitted pulse of energy, i.e., the longer the wavelength, the wider the beam width, and the shorter the wavelength, the narrower the beam width. Therefore, in real aperture (brute force) radars a shorter wavelength pulse will result in improved azimuth resolution. Unfortunately, the shorter the wavelength, the poorer the atmospheric and vegetation penetration capability.

Fortunately, the beam width is also inversely proportional to antenna length (L). This means that the longer the radar antenna, the narrower the beam width and the higher the azimuth resolution. The relationship between wavelength (λ) and antenna length (L) is summarized in Equation 9-10, which can be used to compute the *azimuth resolution* (Henderson and Lewis, 1998):

$$R_a = \frac{S \times \lambda}{L} \qquad (9\text{-}10)$$

where S is the *slant-range distance* to the point of interest. The equation can be used to compute the azimuth resolution at any location between the near- and far-range. For example, consider the conditions shown in Figure 9-11 where the near slant-range is 20 km and the far slant-range is 40 km. Tanks 1 and 2 and tanks 3 and 4 are separated by 200 m. If an X-band radar (3 cm) is used with a 500 cm antenna, then Equation 9-10 can be used to compute the near-range *azimuth resolution*:

$$R_a = \frac{20 \text{ km} \times 3 \text{ cm}}{500 \text{ cm}}$$

$$R_a = \frac{20,000 \text{ m} \times 0.03 \text{ m}}{5 \text{ m}}$$

$$R_a = \frac{600 \text{ m}}{5 \text{ m}}$$

$$R_a = 120 \text{ m}.$$

The far-range azimuth resolution at the 40 km distance is:

$$R_a = \frac{40 \text{ km} \times 3 \text{ cm}}{500 \text{ cm}}$$

$$R_a = \frac{40,000 \text{ m} \times 0.03 \text{ m}}{5 \text{ m}}$$

$$R_a = \frac{1200 \text{ m}}{5 \text{ m}}$$

$$R_a = 240 \text{ m}.$$

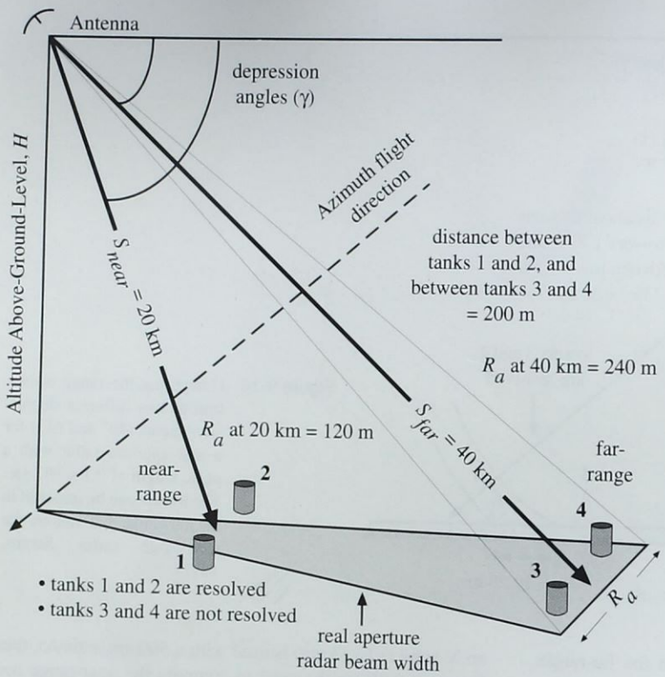

Figure 9-11 Computing the azimuth resolution at two different slant-range distances (20 and 40 km) for a real aperture radar with an X-band wavelength of 3 cm and a 500 cm antenna. The tanks can be resolved in the near-range but not in the far-range.

Tanks 1 and 2 in the near-range would most likely be resolved because the azimuth resolution at this slant-range distance (120 m) is less than the distance between tanks 1 and 2 (200 m). Conversely, tanks 3 and 4 in the far-range would probably not be resolved, because at a slant-range distance of 40 km the azimuth resolution is 240 m, much greater than the 200 m separating the tanks.

There is a trigonometric relationship between the slant-range distance (S) and the depression angle (γ) and the height of the aircraft or spacecraft platform above the local datum, H:

$$S = \frac{H}{\sin\gamma} \quad . \tag{9-11}$$

The equation for computing the azimuth resolution becomes:

$$R_a = \left(\frac{H}{\sin\gamma}\right) \cdot \frac{\lambda}{L} \quad . \tag{9-12}$$

Ideally, one could build an extremely long antenna and place it on an aircraft to achieve very high azimuth resolution. Unfortunately, there is a practical limit (about 2 m) to the size of antenna that can be mounted on an aircraft (although the size is virtually unlimited in outer space!). Fortunately, there are ways to electronically synthesize a longer antenna, which is the heart of the synthetic aperture radar concept to be discussed shortly.

While we have not yet defined how a synthetic aperture radar (SAR) works, it is instructive to point out at this time a significant difference between the computation of the azimuth resolution for a real aperture radar versus a synthetic aperture radar. The equation for the azimuth or along-track resolution for a point target in a synthetic aperture radar (SAR_a) is:

$$SAR_a = \frac{L}{2} \tag{9-13}$$

where L is the antenna length. As Henderson and Lewis (1998) point out,

> This is one of the more incredible equations in the discipline of radar remote sensing. The omission of the slant-range distance (S) from the equation means that the azimuth resolution of a SAR system is independent of range distance or sensor altitude. Theoretically, the spatial resolution in the azimuth direction from a SAR imaging system will be the same from an aircraft platform as it is from a spacecraft. There is no other remote sensing system with this capability!

Equation 9-13, however, is not the only parameter that has an impact in SAR data. The coherent nature of the SAR signal produces speckle in the image. To remove the speckle, the image is usually processed using several *looks*, i.e., an averaging takes place. For example, four looks (N) might be averaged. This dramatically improves the interpretability of the SAR image data. However, the azimuth resolution must be adjusted by the equation:

$$SAR_a = N\left(\frac{L}{2}\right) \quad . \tag{9-14}$$

The SIR-C SAR had a 12 m antenna, which would yield a 6 m along-track resolution if Equation 9-13 were used. However, the speckle in the SIR-C SAR data were processed using $N = 4$ looks to improve the interpretability of the data. Thus, the adjusted azimuth resolution is 24 m.

This discussion first summarized how the range and azimuth resolution are computed for specific locations within the real aperture radar beam swath. Note that the resolution element might have different dimensions, i.e., the range resolution could be 10 m and the azimuth resolution 20 m. Therefore, because scale is constantly changing throughout a real aperture radar image, it is important to be careful when making radargrammetric measurements over large regions. When using such data, it is best to compute the range and azimuth resolution for the major region you are interested in and then make measurements. If a new area is selected for study, then new resolution measurements should be computed before area measurements are obtained.

RADAR Relief Displacement, Image Foreshortening, Layover, Shadows, and Speckle

Geometric distortions exist in almost all radar imagery, including (Ford et al., 1980): foreshortening, layover, and shadowing. When the terrain is flat, it is a straightforward matter to use Equation 9-6 to convert a slant-range radar image into a ground-range radar image that is planimetrically correct in x,y. However, when trees, tall buildings, or mountains are present in the scene, relief displacement in the radar image occurs. In radar relief displacement, the horizontal displacement of an object in the image caused by the object's elevation is in a direction toward the radar antenna (Figure 9-12a). Because the radar image is formed in the

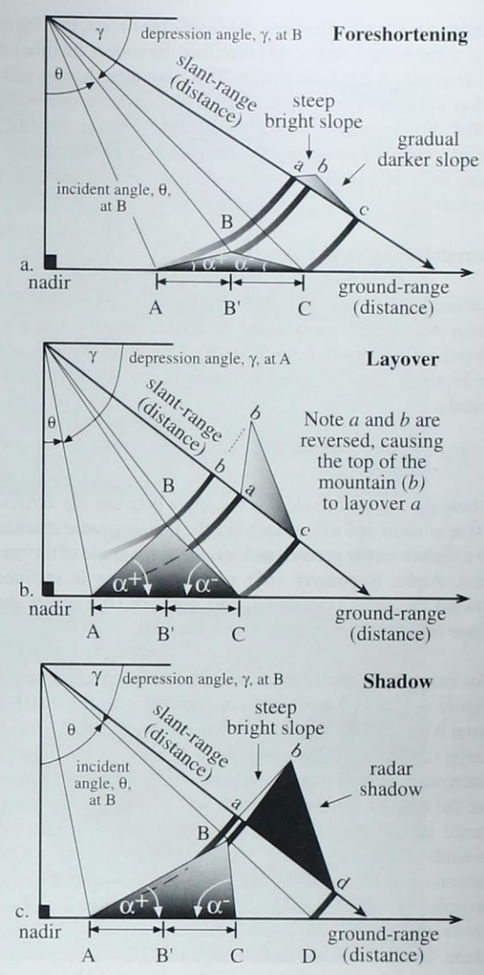

Figure 9-12 a) Radar foreshortening in the slant-range display. Slope AB in the ground-range display and ab in the slant-range display are supposed to be equal as are BC and bc. Instead, slope ab is shorter and steeper while slope bc is more gradual and longer than it should be. b) Image layover of foreslope AB in the slant-range display (ba) caused by the incident angle θ being smaller than the foreslope angle α^+. Slant-range a and b are reversed, causing layover. c) A substantial shadow is produced at bd because the backslope angle (α^-) is greater than the depression angle (γ) (after Ford et al., 1980).

range (cross-track) direction, the higher the object, the closer it is to the radar antenna, and therefore the sooner (in time) it is detected on the radar image. This contrasts sharply with relief displacement in optical aerial photography where the relief displacement is radially outward from the principal point (center) of a photograph. The elevation-induced distortions in radar imagery are referred to as *foreshortening* and *layover.*

Foreshortening and Layover

Basically, all terrain that has a slope inclined toward the radar will appear compressed or foreshortened relative to slopes inclined away from the radar. The effect is illustrated in Figure 9-12a. The foreshortening factor, F_f, is approximately:

$$F_f = \sin(\theta - \alpha) \qquad (9\text{-}15)$$

where the *incident angle* θ is the angle between the vertical plane at nadir and a line that links the imaging radar antenna to a feature on the ground, and α is the slope angle of the surface. Alpha is positive (α^+) where the slope is inclined toward the radar (foreslope), and negative (α^-) where the slope is inclined away from it (backslope).

For example, consider the relatively low relief mountain in Figure 9-12a. It is perfectly symmetrical with the distance from AB' and B'C being equal when plotted in the ground-range (i.e., on a quality planimetric map). A single pulse of microwave energy illuminating the terrain will first encounter the base of the mountain (*A*) and record it in the slant-range image at *a*. Because the top of the mountain (*B*) extends above the terrain and is relatively close to the antenna, it is recorded at *b*. The base of the mountain at *C* is recorded at *c* in the slant-range display. The higher the object above the terrain, the more foreshortening that will take place. In this case, the radar image will have a very bright short foreslope and a darker backslope. It would be difficult to make a map of mountainous features using this radar image because the top of the mountain, even though it was not very high, is displaced from its true ground-range planimetric position in the radar image, i.e., *ab* does not equal *bc*. Foreshortening is influenced by the following factors:

- *object height*: The greater the height of the object above local datum, the greater the foreshortening.

- *depression angle* (or *incident angle*): The greater the depression angle (γ) or smaller the incident angle (θ), the greater the foreshortening. A good example is found in Figure 9-13a,b where the ERS-1 sensor with its large 67° depression angle and its 23° incident angle introduces more foreshortening than the JERS-1 radar with its 51° depression angle and 39° incident angle. Also consider the foreshortened cinder cone in Arizona when recorded on a radar image versus a conventional vertical aerial photograph (Figure 9-13c,d).

- *location of objects in the across-track range:* Features in the near-range portion of the swath are generally foreshortened more than identical features in the far-range. Foreshortening causes features to appear to have steeper slopes than they actually have in nature in the near-range of the radar image and to have shallower slopes than they actually have in the far-range of the image (Campbell, 1996).

Image *layover* is an extreme case of image foreshortening. It occurs when the incident angle (θ) is smaller than the foreslope (α^+), i.e., $\theta < \alpha^+$. This concept is illustrated in Figure 9-12b. In this case, the mountain has so much relief that the summit (*B*) backscatters energy toward the antenna before the pulse of energy even reaches the base of the mountain (*A*). Remember that in terms of planimetric distance from the nadir point directly beneath the aircraft, the base of the mountain (*A*) is much closer than the summit (*B*), as documented by the ground-range distance display. However, because the mountain summit (*B*) reflects the incident microwave energy sooner than the base of the mountain (*A*), the summit (*b*) in the slant-range radar image actually *lays over* (hence the terminology) the base of the mountain recorded on the radar image at *a*. Once again, the summit of the mountain (*a*) is significantly displaced from its true planimetric position. This distortion cannot be corrected even when the surface topography is known. Great care must be exercised when interpreting radar images of mountainous areas where the thresholds for image layover exist. The bright white ridges in Figure 9-14 represent severe SIR-C L-band (HH) radar layover in the San Gabriel Mountains just east of Los Angeles, CA.

Shadows

Shadows in radar images can enhance the geomorphology and texture of the terrain. Shadows can also obscure the most important features in a radar image, such as the information behind tall buildings or land use in deep valleys. If certain conditions are met, any feature protruding above the local datum can cause the incident pulse of microwave energy to reflect all of its energy on the foreslope of the object and produce a black shadow for the backslope. A backslope is in radar shadow when its angle (α^-) is steeper than the depression angle (γ), i.e., $\alpha^- > \gamma$ (Figure 9-12c). If the backslope

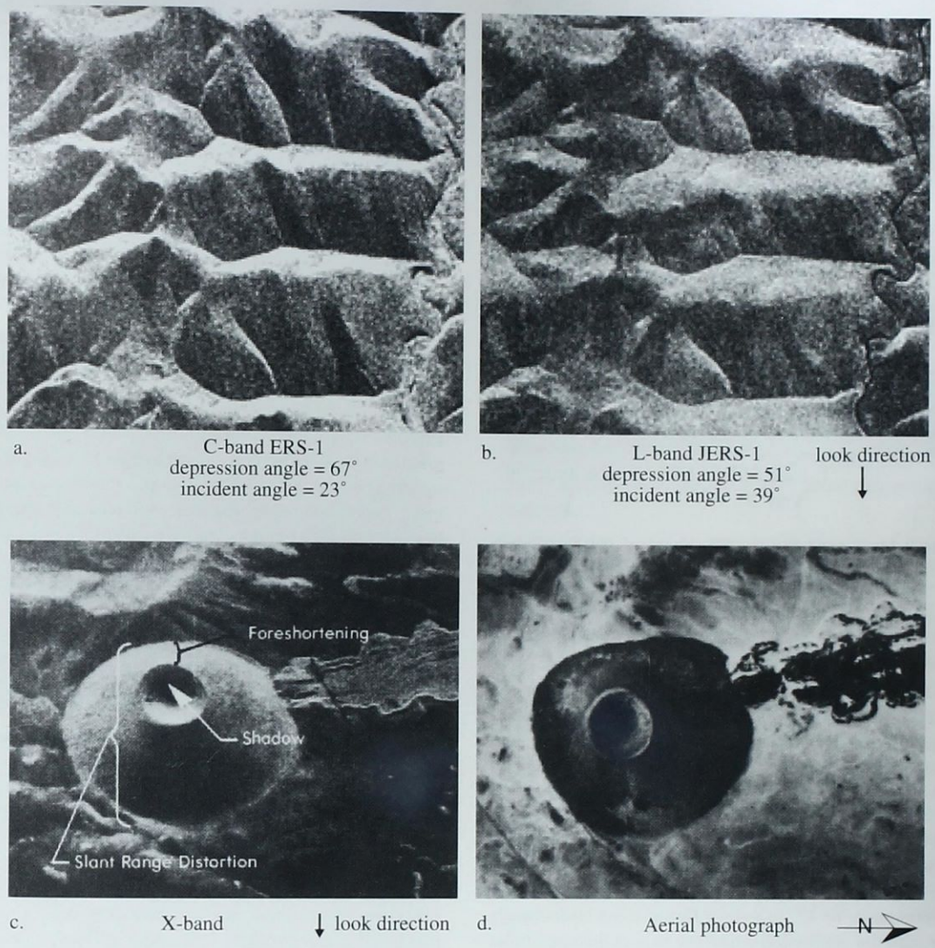

Figure 9-13 a) The C-band ERS-1 image of the White Mountains exhibits substantial foreshortening due to the satellite SAR's small incident angle (courtesy Alaska SAR Facility; © 1992, European Space Agency). b) The L-band JERS-1 image with a larger incident angle has significantly less image foreshortening (courtesy Alaska SAR Facility; © NASDA). c) X-band aircraft synthetic aperture radar (SAR) image of a cinder cone in Arizona. The shape of the basically cylindrical cinder cone is distorted in the slant-range look direction, appearing more elliptical in shape than it does in the aerial photograph. Foreshortening (relief displacement toward the radar antenna) occurs in the near-range. There is also a dark shadow under the rim of the crater at the top of the cone. d) Vertical panchromatic aerial photograph of SP Mountain, AZ (courtesy of Eric Kasischke, ERIM International, Inc.).

Figure 9-14 L-band SIR-C (HH) image of the San Gabriel Mountains and a portion of the city of Pasadena. Extensive layover is found in the mountainous terrain, causing the ridge lines to be displaced toward the antenna (courtesy NASA Jet Propulsion Lab).

equals the depression angle ($\alpha^- = \gamma$), then the backslope is just barely illuminated by the incident energy. This is called grazing illumination because the radar pulse just grazes the backslope. The backslope is fully illuminated when it is less than the depression angle ($\alpha^- < \gamma$).

Figure 9-12c demonstrates how a large shadow from a relatively steep backslope might be produced. In this case, we have a backslope of approximately 85° ($\alpha^- = 85°$) and a depression angle of 45° ($\gamma = 45°$). Because the backslope is greater than the depression angle, we expect this area to be in shadow. In fact, this is the case with the terrain surface *BCD* in the ground-range being in complete shadow in the slant-range radar image display (*bd*). In the ground-range display the distance from the summit at B to the back base of the mountain at C is relatively short. But in the slant-range radar image, *bd* is very long. This particular radar image would also experience image foreshortening (but not layover because *A* is recorded by the antenna before *B*) and have a very bright return from the foreslope.

Some important characteristics of radar shadows are:

- Unlike aerial photography, where light may be scattered into the shadow area and then recorded on film, there is no information within the radar shadow area. It is black.

- Two terrain features (e.g., mountains) with identical heights and fore- and backslopes may be recorded with entirely different shadows, depending upon where they are in the across-track. A feature that casts an extensive shadow in the far-range might have its backslope completely illuminated in the near-range.

- Radar shadows occur only in the cross-track dimension. Therefore, the orientation of shadows in a radar image provides information about the look direction and the location of the near- and far-range.

Shadows in radar imagery are valuable when evaluating geomorphic characteristics. Radar shadows often function like low Sun-angle photography, enhancing lineaments and other geologic conditions. Terrain information such as topographic height, slope, etc., can be used to configure radar overflights or, purchase radar data that have the most appropriate depression angles and near- and far-range characteristics to emphasize terrain shadows.

Speckle

Speckle is a grainy salt-and-pepper pattern in radar imagery (Figure 9-15) that is present due to the coherent nature of the radar wave, which causes random constructive and destructive interference, and hence random bright and dark areas in a radar image. The speckle can be reduced by processing separate portions of an aperture and recombining these portions so that interference does not occur (Kasischke et al., 1984). As previously mentioned, this process, called multiple *looks* or noncoherent integration, produces a more pleasing appearance, and in some cases may aid in interpretation of the image but at a cost of degraded resolution. For example, consider the radar imagery in Figure 9-15 which was processed using 1-look, 4-looks, and 16-looks. Most interpreters would prefer working with the 4- or 16-look imagery.

Synthetic Aperture Radar Systems

A major advance in radar remote sensing has been the improvement in azimuth resolution through the development of *synthetic aperture radar* (SAR) systems. Remember, in a real aperture radar system that the size of the antenna (*L*) is inversely proportional to the size of the angular beam width (Equation 9-10). Therefore, great improvement in azimuth

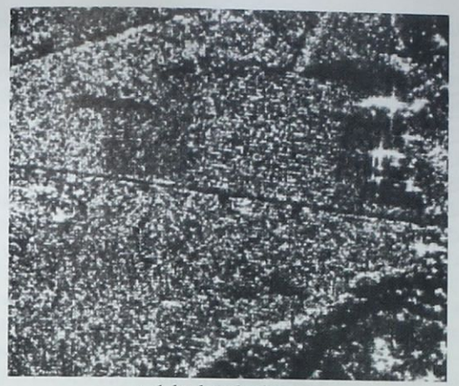

a. 1-look radar image

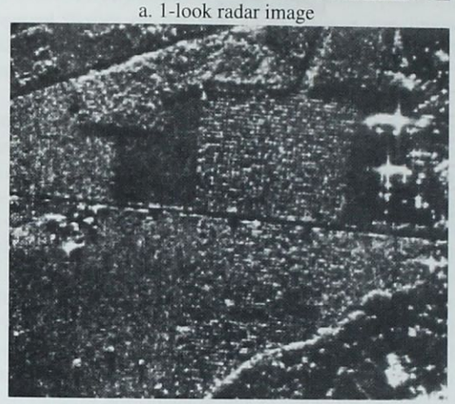

b. 4-look radar image

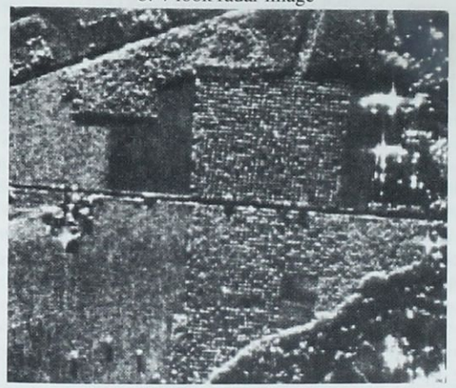

c. 16-look radar image

Figure 9-15 Radar speckle reduction using multiple-look techniques (courtesy of Eric Kasischke, ERIM International, Inc.).

resolution could be realized if a longer antenna were used. Engineers have developed procedures to *synthesize* a very long antenna electronically. Like a brute force or real aperture radar, a synthetic aperture radar also uses a relatively small antenna (e.g., 1 m; refer to Figure 9-1) that sends out a relatively broad beam perpendicular to the aircraft. The major difference is that a greater number of additional beams are sent toward the object. Doppler principles are then used to monitor the returns from all these additional microwave pulses to synthesize the azimuth resolution to become one very narrow beam.

The *Doppler principle* states that the frequency (pitch) of a sound changes if the listener and/or source are in motion relative to one another. For example, an approaching train whistle will have an increasingly higher frequency pitch as it approaches. This pitch will be highest when it is directly perpendicular to the listener (receiver). This is called the point of zero Doppler. As the train passes by, its pitch will decrease in frequency in proportion to the distance it is from the listener (receiver). This principle is applicable to all harmonic wave motion, including the microwaves used in radar systems.

Figure 9-16 depicts the Doppler frequency shift due to the relative motion of a terrain object at times *n, n+1, n+2, n+3,* and *n+4* through the radar beams due to the forward motion of the aircraft. The Doppler frequency diagram reveals that the frequency of the energy pulse returning from the target increases from a minimum at time *n* to a maximum at point *n+3,* normal (at a right angle) to the aircraft. Then, as the target recedes from *n+3* to *n+4*, the frequency decreases.

How is a synthetic aperture image actually produced? A long antenna can be synthesized using a short antenna by taking advantage of the aircraft's motion and the Doppler principle. It is assumed that the terrain is stable and *not* moving. It is also assumed that the object of interest remains a fixed distance away from the aircraft's flightline. As the aircraft flies along a straight line, a short antenna sends out a series of microwave pulses at regular intervals (Jensen et al., 1977). As an object (black dot) enters the antenna's beam (Figure 9-16a), it backscatters a portion of the pulse it receives toward the antenna. At some point in the aircraft's path the object will be an integral number of microwave wavelengths away; between those points it will not be. For example, in (a) we see that the object is first 9 wavelengths away, then 8 (b), then 7 (c), then 6.5 (d), at which point the object is at a right angle to the antenna, i.e., the shortest distance and area of zero Doppler shift. From then on the distance between the aircraft and the object will be increasing, i.e., perhaps 7 wavelengths away at location (e). The antenna receives the

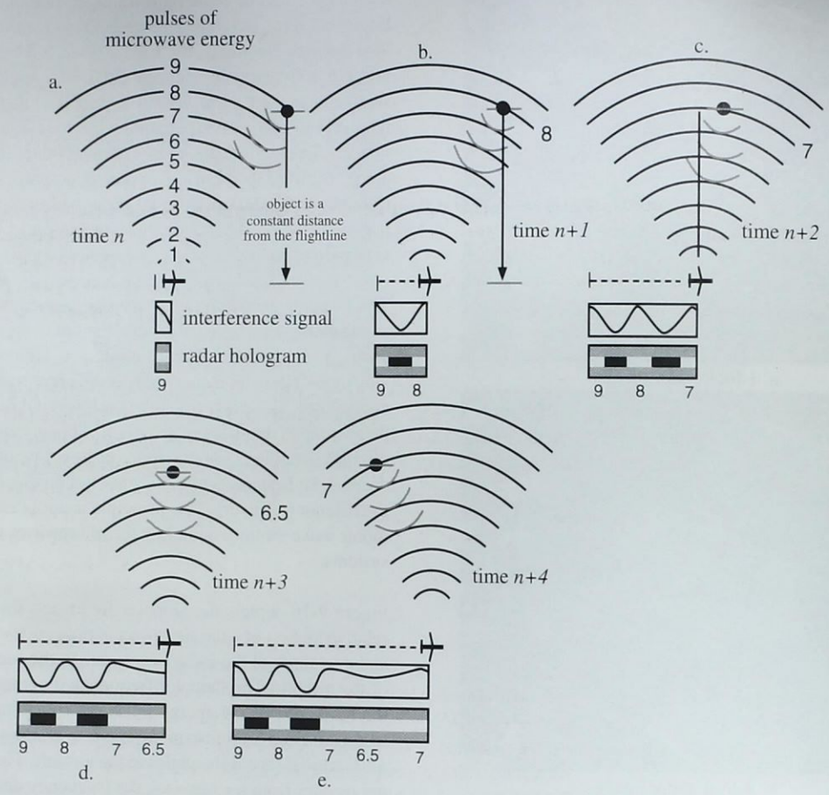

Figure 9-16 A long antenna can be synthesized by a short antenna (e.g., 1 m long) by taking advantage of the aircraft's motion and Doppler principles. As the craft flies along a straight line, a mounted short real antenna sends out a series of pulses at regular intervals. Each pulse consists of a train of coherent microwaves. Although the length of the pulses determines the resolution across the track, it is the wavelength of the microwave radiation that determines the resolution along the track. As an object (black dot) enters the antenna's beam (*a*), it reflects a portion of the pulses it receives back toward the antenna. At some point in the aircraft's path the object is an integral number of microwave wavelengths away; between these points it will not be. For example, in the illustration the object is first 9 wavelengths away at *a*, then 8 at *b*, then 7 at *c*, then 6.5 at *d*, where the object is at right angles to the antenna. From then on, the crest is increasing its distance from the object, e.g., point *e*. The antenna receives the series of reflected waves and electronically combines them with a train of reference wavelengths (not shown), causing the two series of oscillations to interfere. The interference signal emerges as a voltage that controls the brightness of a spot scanning across a cathode-ray tube. At the times that a returned pulse coincides with a reference pulse, the interference is constructive; the voltage will be high and the moving spot will be bright. At the times that the phase of the returned wavelength does not coincide with the phase of the reference frequency the interference is destructive; the voltage will be low and the moving spot will be dim. The moving spot thus traces out a series of light and dark dashes of unequal length that are recorded on a strip of data film moving at a velocity proportional to the velocity of the aircraft (after Jensen et al., 1977; Kasischke et al., 1984).

series of reflected waves (gray lines in illustrations a – e) and electronically combines them with a train of reference wavelengths (not shown), causing the two series of oscillations to interfere. The interference signal emerges as a voltage that controls the brightness of a spot scanning across the screen of a cathode-ray tube. When the returned pulse coincides with a reference pulse, the interference is constructive; the voltage will be high and the moving spot will be bright. When the phase of the returned wavelength does not coincide with the phase of the reference frequency, the interference is destructive; the voltage will be low and the moving spot will be dim or dark. The moving spot thus tracks out a series of light and dark dashes of unequal length that are recorded on a strip of data film moving at a velocity proportional to the velocity of the aircraft. The series of opaque and transparent dashes on the film are actually a one-dimensional interference pattern; the film on which they are recorded is a *radar hologram.*

When the developed hologram is illuminated by a source of coherent light (Figure 9-17a), each transparent dash functions as a separate source of coherent light. Below the hologram there will be a single point where the resulting light waves all constructively interfere. In this example, the 9th wavelength of light (thick curved lines) from the transparent dash created by the 9th microwave will meet the 8th wavelength of light (regular lines) from the transparent dash created by the 8th microwave, and both will meet the 7th wavelength of light (thin curves) from the transparent dash created by the 7th microwave and so on (only the 9th, 8th, and 7th patterns are shown in this example for clarity). At that one point, light from the entire length of the interference pattern is focused to form a miniature image of the original object. Figure 9-17b demonstrates how the holographic image is reconstructed and recorded on film. After processing the negative film to become a positive print, the radar image is ready for analysis.

The record of Doppler frequency enables the target to be resolved on the image film as though it was observed with an antenna of length *L*, as shown in Figure 9-18 (Leberl, 1990; Sabins, 1997). This synthetically lengthened antenna produces the effect of a very narrow beam with constant width in the azimuth direction, shown by the shaded area in Figure 9-18. For both real and synthetic aperture systems, range resolution is determined by pulse length and depression angle. Generally, synthetic aperture images are higher in azimuth resolution than real aperture radars.

The aforementioned method is often called synthetic aperture radar *optical correlation* because of all the precision optics utilized. It is also possible to use *SAR digital correlation* techniques to record and process the amplitude and phase history of the radar returns. Digital correlation does not produce an intermediate radar film. The digital process is computation intensive. Major advantages of digital correlation include the ability to 1) perform both radiometric and geometric corrections rapidly during onboard processing (good for emergencies such as oil spills, floods, fires, etc.), 2) telemeter the processed radar data directly to the ground to support real-time decision making, and/or 3) store the digitally processed SAR data on high-density digital tapes (HDDTs) for subsequent digital processing on the ground. Many of the commercial (e.g., Intermap Star 3*i*) and government SARs (e.g., RADARSAT) use digital SAR correlation techniques.

The Radar Equation

The following discussion provides additional quantitative information about the radar signal. A radar image is a two-dimensional representation of the power (or voltage) returned to the radar from a specific area on the ground presented as a picture element (pixel). This returned power is usually quantized to a radiometric scale of 256 values (8 bits) for presentation on image processing systems (Leberl, 1990). RADARSAT is quantized to 11 bits. To understand how to interpret radar images, we should understand the nature of the power scattered back toward the radar antenna. In the most simple case, this can be stated verbally as suggested by Moore (1983):

$$\begin{pmatrix}\text{Power}\\ \text{received}\end{pmatrix} = \begin{pmatrix}\text{Power per unit}\\ \text{area at target}\end{pmatrix} \times \begin{pmatrix}\text{Effective scattering}\\ \text{area of the target}\end{pmatrix}$$

$$\times \begin{pmatrix}\text{Spreading loss of}\\ \text{reradiated signal}\end{pmatrix} \times \begin{pmatrix}\text{Effective antenna}\\ \text{receiving area}\end{pmatrix}$$

where the power per unit area at the receiver is the energy scattered back from the terrain — *backscatter.* The spreading loss occurs because the signal starts from the backscattering point source on the ground (e.g., a large rock) and spreads out in all directions, so that the power per unit area is less at a greater distance than it would be near the scatterer. Therefore, the strength of the backscatter toward the receiver is a product of the power per unit area illuminating the target, times the effective scattering area of the target, and then the retransmission of this wave back toward the receiving antenna. The actual size of the receiving antenna also makes a difference.

The fundamental radar equation is derived by combining these word quantities to create the mathematical expression (Moore, 1983; Kasischke et al., 1984):

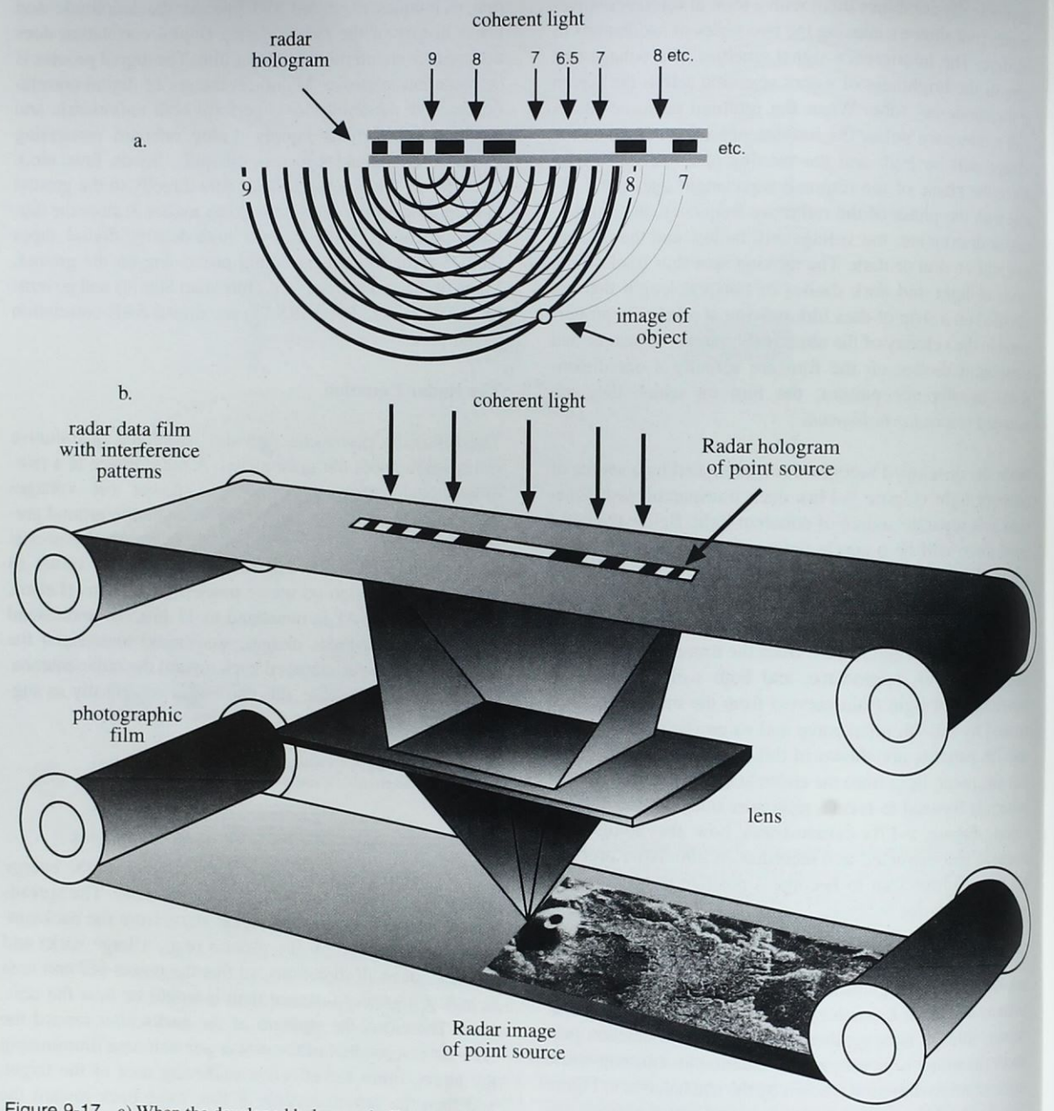

Figure 9-17 a) When the developed hologram is illuminated by laser coherent light, each transparent dash acts as a separate source of coherent light. Below the hologram there is a single point where the resulting light waves all constructively interfere. Here the 9th wavelength of light from the transparent dash created by the 9th microwave will meet the 8th wavelength of light from the transparent dash created by the 8th microwave, and both will meet with the 7th wavelength of light from the transparent dash created by the 7th microwave. At that one point light from the entire length of the interference pattern is focused to form a miniature image of the original object. b) As the data film is advanced through the beam of laser light, the reconstructed image is recorded on another moving strip of film. Because the data film is holographic only in the along-track coordinate, the images in the across-track coordinate must be focused with a cylindrical lens (after Jensen et al., 1977).

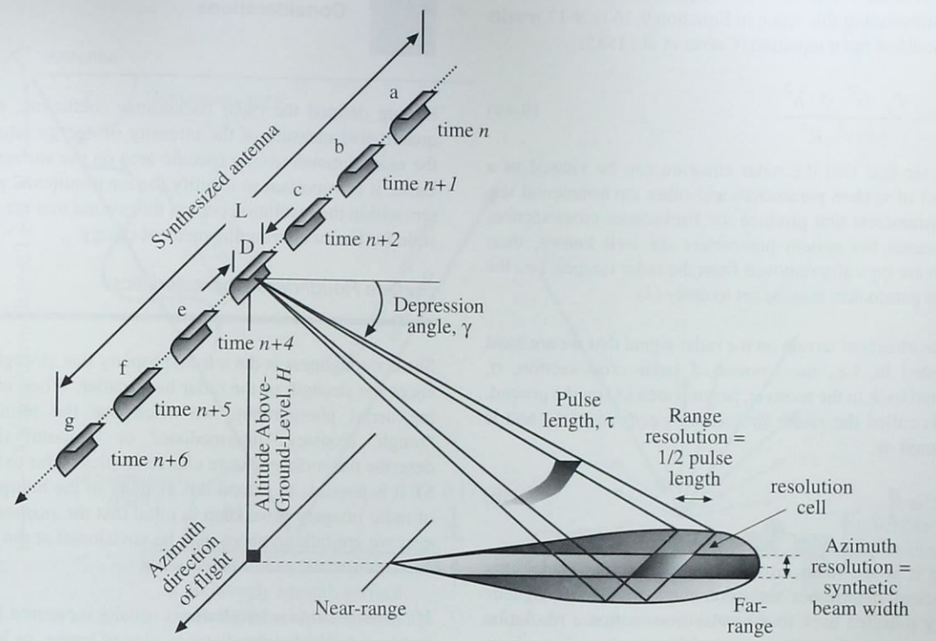

Figure 9-18 A synthetic antenna of length L is produced by optically or digitally processing the phase histories of microwave radar returns sent and received by a real antenna of length D sent at times n. The synthetic aperture radar has a range resolution that is approximately equal to half the pulse length. Note how the azimuth resolution remains constant from the near-range to the far-range (after Sabins, 1997).

$$P_r = \frac{P_t \cdot G_t \cdot \sigma \cdot A_r}{(4\pi)^2 \cdot R^4} \tag{9-16}$$

where P_r is power received, P_t is the power transmitted toward the target, G_t is the gain of the antenna in the direction of the target, R is the range distance from the transmitter to the target, σ is the effective backscatter area of the target (often called the radar cross-section), and A_r is the area of the receiving antenna. This equation can be broken down into seven parts for even more clarity:

$$P_r = P_t \cdot G_t \cdot \frac{1}{4\pi R^2} \cdot \sigma \cdot \frac{1}{4\pi R^2} \cdot A_r \tag{9-17}$$

$$1 = 2 \cdot 3 \cdot 4 \cdot 5 \cdot 6 \cdot 7$$

The power received [1] by the radar system, P_r, is a function of a pulse of electromagnetic energy, P_t [2], that has been focused down to an angular beam width by the antenna so that the flux becomes higher by a factor [3] of G_t over a spherically expanding wave [4]. The focused energy illuminates an *area* on the ground that has a cross-section of σ [5]. The *radar cross-section* is defined as the equivalent of a perfectly reflecting area that reflects isotropically (spherically). The energy backscattered from the ground once again spherically expands from the source [6]. Finally, the receiving antenna area (A_r) intercepts a portion of the reflected wave and records it [7].

Most radars use the same antennas for transmitting (A_t) and receiving (A_r). Consequently, the gain factors of the antennas may be combined using the relationship between gain and receiving aperture as (Moore, 1983):

$$G = G_t = G_r = \frac{4\pi A_r}{\lambda^2} \tag{9-18}$$

where λ is the wavelength (or frequency) of the radar system. Substituting this value in Equation 9-16 or 9-17 results in a modified radar equation (Carver et al., 1985):

$$P_r = \frac{P_t \cdot G^2 \cdot \sigma \cdot \lambda^2}{(4\pi)^3 \cdot R^4}. \qquad (9\text{-}19)$$

Thus, we find that the radar equation can be viewed as a product of system parameters and other environmental terrain parameters that produce the backscatter cross-section, σ. Because the system parameters are well known, their effects are typically removed from the radar images, i.e., the system parameters may be set to unity (1).

It is the effects of terrain on the radar signal that we are most interested in, i.e., the amount of radar cross-section, σ, reflected back to the receiver, per unit area (*A*) on the ground. This is called the *radar backscatter coefficient* (σ°) and is computed as:

$$\sigma^\circ = \frac{\sigma}{A} \qquad (9\text{-}20)$$

where σ is the radar cross-section. The radar backscatter coefficient determines the percentage of electromagnetic energy reflected back to the radar from within a resolution cell, e.g., 10 x 10 m. The actual σ° for a surface depends on a number of terrain parameters, like geometry, surface roughness, moisture content, and the radar system parameters (wavelength, depression angle, polarization; Leberl, 1990). σ° is a dimensionless quantity characteristic of the scattering behavior of all the elements contained in a given ground cell. Because σ° can vary over several orders of magnitude, it is expressed as a logarithm with units of decibels (dB) that usually range from -5 to +40 dB.

The total radar cross-section of an area (*A*) on the ground therefore becomes ($\sigma^\circ A$), and the final form of the radar equation for an area-extensive target becomes (Henderson and Lewis, 1998):

$$P_r = P_t(\sigma^\circ A)\left(\frac{G^2 \cdot \lambda^2}{(4\pi)^3 \cdot R^4}\right). \qquad (9\text{-}21)$$

A digital SAR image is created that consists of a two-dimensional array (matrix) of picture elements (pixels) with the intensity (called the brightness) of each pixel proportional to the power of the microwave pulse reflected back from the corresponding ground cell (Waring et al., 1995). The reflected radar signal is proportional to the backscattering coefficient (σ°) of a given ground cell.

RADAR Environmental Considerations

Having defined the radar backscatter coefficient, σ°, as a quantitative measure of the intensity of energy returned to the radar antenna from a specific area on the surface of the Earth, it is important to identify the environmental parameters within the resolution cell on the ground that are responsible for backscattering the incident energy.

Surface Roughness Characteristics

Surface roughness is the terrain property that strongly influences the strength of the radar backscatter. When interpreting aerial photography, we often use the terminology "rough" (coarse), "intermediate," or "smooth" (fine) to describe the surface texture characteristics (refer to Chapter 5). It is possible to extend this analogy to the interpretation of radar imagery if we keep in mind that the *surface roughness* we are talking about may be envisioned at the *microscale*, *mesoscale*, and/or *macroscale*.

Microscale surface roughness is usually measured in centimeters (i.e., the height of stones, size of leaves, or length of branches in a tree) and not in hundreds or thousands of meters as with topographic relief or mountains. The amount of microwave energy backscattered toward the sensor based on microscale components is a function of the relationship between the wavelength of the incident microwave energy (λ), the depression angle (γ), and the local height of objects (*h* in cm) found within the resolution cell being illuminated. We may use the *modified Rayleigh criteria* to predict what the Earth's surface will look like in a radar image if we know the microscale surface roughness characteristics and the radar system parameters (λ,γ,*h*) mentioned (Peake and Oliver, 1971). For example, one would expect that an area with *smooth surface roughness* would send back very little backscatter toward the antenna, i.e., it acts like a specular reflecting surface, where most of the energy bounces off the terrain away from the antenna (Figure 9-19a). The small amount of backscattered energy returned to the antenna is recorded and shows up as a dark area on the radar image. The quantitative expression of this *smooth criteria* is:

$$h < \frac{\lambda}{25 \sin\gamma}. \qquad (9\text{-}22)$$

To illustrate we will compute what the local height (*h*) of objects (e.g., grass and rocks in this example) must be in

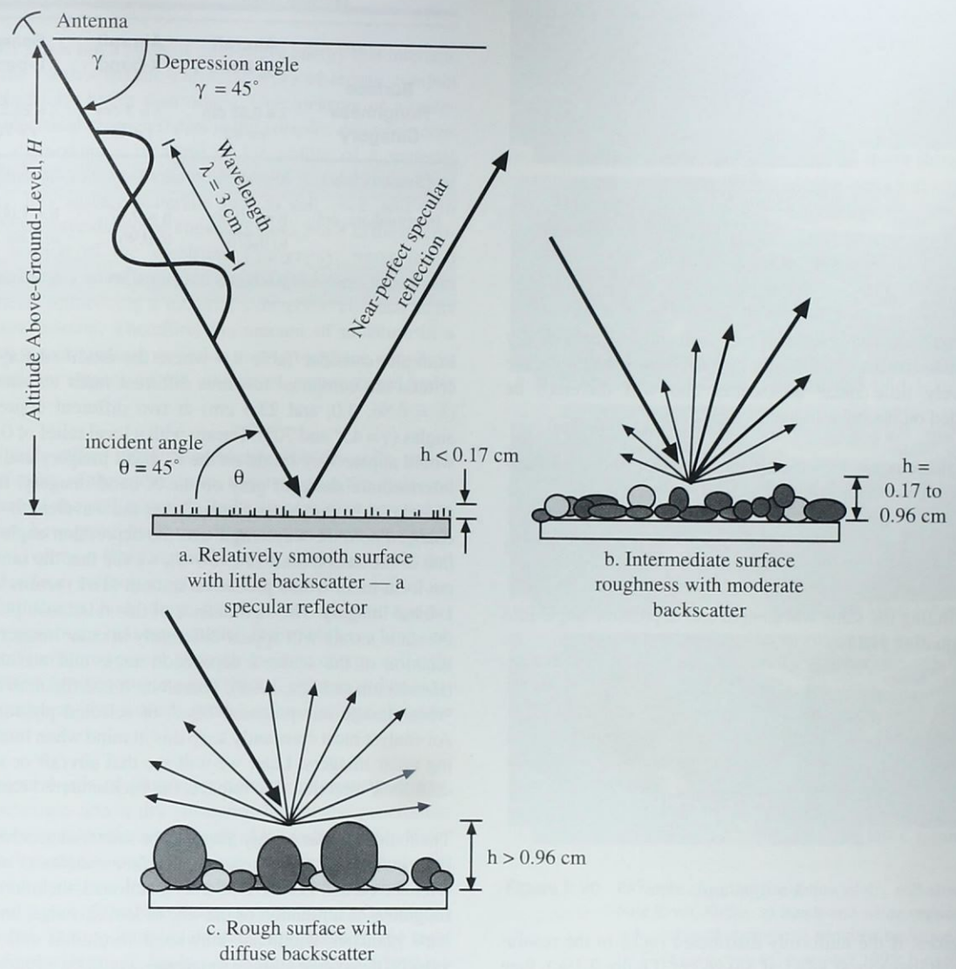

Figure 9-19 Expected surface roughness backscatter from terrain illuminated with 3 cm wavelength microwave energy. a) With a depression angle of 45° and a local relief of < 0.17 cm, the terrain represents a relatively smooth surface and should produce very little backscatter toward the sensor. This specular reflector will appear dark on the radar image. b) Local relief from 0.17 – 0.96 cm represents intermediate surface roughness and should produce a medium gray response on the radar image. c) When the local surface roughness relief is > 0.96 cm, a rough surface exists that will produce very diffuse backscatter. This diffuse reflector will produce a bright return on the radar image due to the large amount of microwave energy reflected back toward the antenna.

order to produce a smooth (dark) radar return when an X-band (λ = 3.0 cm) radar is used with a depression angle (γ) of 45° (Figure 9-19a). Substituting these values into Equation 9-22 yields:

$$h < \frac{3\text{cm}}{25\sin 45°}$$

$$h < \frac{3\text{cm}}{25 \times 0.70711}$$

$$h < 0.17 \text{ cm}.$$

This means that a resolution cell uniformly filled with dry grass that has a surface height of < 0.17 cm should produce relatively little radar backscatter and will therefore be recorded on the radar image in a dark tone.

A bright return is expected if the following modified Rayleigh *rough criteria* are used:

$$h > \frac{\lambda}{4.4\sin\gamma}. \qquad (9\text{-}23)$$

Substituting the same wavelength and depression angle into this equation yields:

$$h > \frac{3\text{cm}}{4.4\sin 45°}$$

$$h > \frac{3\text{cm}}{4.4 \times 0.70711}$$

$$h > 0.96 \text{ cm}.$$

Therefore, if the uniformly distributed rocks in the resolution cell had a local relief of > 0.96 cm (Figure 9-19c), then a strong return from the terrain would be expected and would be recorded as a bright tone in the radar image.

If the terrain were composed of rocks with local relief between 0.17 and 0.96 cm, it would be considered to have an *intermediate surface roughness* for this combination of wavelength and depression angle and would produce an intermediate tone of gray on the radar image.

It is important to remember that the radar backscatter is dependent on the wavelength and the depression angle. For

Table 9-4. Modified Rayleigh Surface Roughness Criteria for Three Different Radar Systems at Two Different Depression Angles

Surface Roughness Category	Aircraft K_a-band λ = 0.86 cm γ = 45°	Aircraft X-band λ = 3 cm γ = 45°	Seasat L-band λ = 23.5 cm γ = 70°
Smooth, cm	h < 0.048	h < 0.17	h < 1.00
Intermediate, cm	h = 0.048 to 0.276	h = 0.17 to 0.96	h = 1.00 to 5.68
Rough, cm	h > 0.276	h > 0.96	h > 5.68

example, consider Table 9-4 where the modified Rayleigh criteria are computed for three different radar wavelengths (λ = 0.86, 3.0, and 23.5 cm) at two different depression angles (γ = 45° and 70°). Terrain with a local relief of 0.5 cm would appear very bright on the K_a-band imagery and as an intermediate shade of gray on the X-band imagery. In this case the only parameter changed was the wavelength. If we changed both the wavelength and the depression angle to be that of the Seasat SAR (Table 9-4), we see that the same 0.5 cm local relief would produce a smooth (dark) return in this L-band imagery. The significance of this relationship is that the same terrain will appear differently in radar imagery as a function of the sensor's depression angle and wavelength (Henderson and Xia, 1998). Therefore, it is difficult to create "radar image interpretation keys" of selected phenomena. An analyst must constantly keep this in mind when interpreting radar imagery. Later we will see that aircraft or spacecraft look-direction also impacts the backscattered energy.

The incident radar energy may also be scattered according to both *mesoscale* and *macroscale surface roughness* criteria (Henderson and Lewis, 1998). As mentioned, the microscale roughness is a function of the size of leaves, twigs, and perhaps branches within an individual resolution cell. Conversely, mesoscale surface roughness would be a function of the characteristics within numerous resolution cells, perhaps covering the entire forest canopy. Based on this logic, we would expect forest canopies to generally show up with a more coarse texture than grasslands when recorded in the same image at the same depression angle and wavelength. Finally, *macroscale* roughness would be influenced greatly by how the entire forest canopy is situated on the hillside. Macroscale roughness is significantly influenced by the topographic slope and aspect of the terrain with the existence or absence of shadows playing a very important role in creating image surface roughness.

Electrical Characteristics (Complex Dielectric Constant) and the Relationship with Moisture Content

A radar sends out a pulse of microwave energy that interacts with the Earth's terrain. Different types of terrain conduct this electricity better than others. One measure of a material's electrical characteristics is the *complex dielectric constant,* defined as a measure of the ability of a material (vegetation, soil, rock, water, ice) to conduct electrical energy. Dry surface materials such as soil, rock, and even vegetation have dielectric constants from 3 to 8 in the microwave portion of the spectrum. Conversely, water has a dielectric constant of approximately 80. The most significant parameter influencing a material's dielectric constant is its *moisture content*. Therefore, the amount of moisture in a soil, on a rock surface, or within vegetative tissue may have a significant impact on the amount of backscattered radar energy.

Moist soils reflect more radar energy than dry soils, which absorb more of the radar wave, depending on the dielectric constant of the soil material. Radar images may be used to estimate *bare* ground soil moisture content when the terrain is devoid of most other material such as plants and rocks and has a uniform surface roughness. The amount of soil moisture influences how deep the incident electromagnetic energy penetrates into the material. If the soil has a high surface soil moisture content, then the incident energy will only penetrate a few centimeters into the soil column and be scattered more at the surface producing a stronger, brighter return.

The general rule of thumb for how far microwave energy will penetrate into a dry substance is that the penetration should be equal to the wavelength of the radar system. However, active microwave energy may penetrate extremely dry soil several meters. For example, Figure 9-20 depicts four views of a part of the Nile River, near the Fourth Cataract in the Sudan. The top image is a photograph taken by the crew of the Space Shuttle *Columbia* in November 1995. The three radar images were acquired by the Shuttle Imaging Radar C/X-band Synthetic Aperture Radar (SIR-C/X-SAR) onboard Space Shuttle *Endeavor* in April 1994; C-band HV, L-band HV, and L-band HH. Each radar image provides some unique information about the geomorphology of the area. The thick white band in the top right of the radar image is an ancient channel of the Nile that is now buried under layers of sand. This channel cannot be seen in the photograph, and its existence was not known before the radar imagery was processed. The area to the left in both images shows how the Nile is forced to flow through a set of fractures that causes

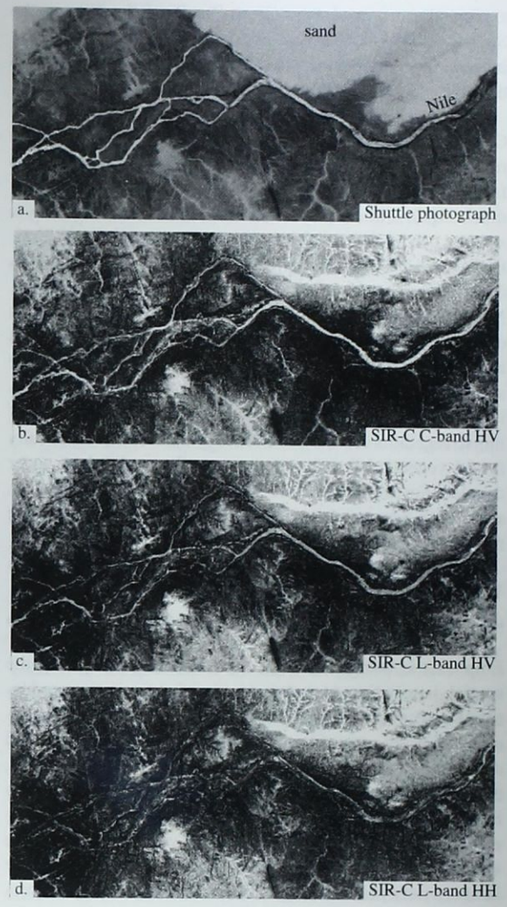

Figure 9-20 Example of radar penetration of dry soil along the Nile River, Sudan. a) Black-and-white version of a color-infrared photograph acquired by Space Shuttle *Columbia* crew in November 1995; b-d) SIR-C/X-SAR images acquired by the Space Shuttle *Endeavor* in April 1994. Subtle, different information is recorded in each of the three radar images. Each reveals an ancient, previously unknown channel of the Nile. Radar brightness values are inverted in these examples (courtesy NASA Jet Propulsion Laboratory).

the river to break up into smaller channels, suggesting that the Nile has only recently established this course. The radar images have allowed scientists to develop new theories to

explain the origin of the "Great Bend" of the Nile in the Sudan. Color Plate 9-1 is a color composite of the three radar images. It provides more revealing visual information about the regional geomorphology.

Ocean surfaces have a very high dielectric constant with most of the radar energy being reflected at the water's surface. The dielectric constant of snow depends upon how much liquid water is in the snow. Thus, microwave remote sensing can be used to determine snow water content. Similarly, there are differences in the dielectric constants of ice, depending upon age, degree of compaction, and type of ice. Microwave remote sensing has been useful for the extraction of these biophysical variables. Finally, healthy agricultural crops and forest canopy leaves often have relatively large surface areas and high moisture content (high relative turgidity). Therefore, it is not surprising that dense canopies of moist vegetation reflect radar energy well. In effect, a fully turgid vegetated forest canopy acts like a cloud of water droplets hovering above the surface of the Earth. Also, the steeper the depression angle, the greater the sensitivity of the radar to soil and vegetation moisture content.

Vegetation Response to Microwave Energy

Emphasis is being placed on quantitatively monitoring the spatial distribution, biomass, gross and net primary productivity, and condition of global vegetation communities, especially forests (approximately 33 percent of the Earth's land surface), semi-arid ecosystems of grassland/steppe/desert, agricultural land (10 percent), and wetlands. Scientists are interested in how energy and matter move within these vegetated ecosystems. Many of these vegetated areas are shrouded in perennial cloud cover. Synthetic aperture radar imagery may provide some of the following vegetation biophysical parameters (Carver, 1988):

- canopy water content,
- vegetation type,
- biomass by component (foliage, higher-order stems and main stem), and
- canopy structure (including green leaf area index), leaf orientation, main stem (trunk) geometry and spatial distribution, stem, branch size, and angle distributions.

Any plant canopy (forest, agriculture, grassland, etc.) may be thought of as a seasonally dynamic three-dimensional water-bearing structure consisting of foliage components (leaves) and woody components (stems, trunk, stalks, and branches). Remote sensing systems such as the Landsat Thematic Mapper, SPOT, or aerial photography sense reflected optical wavelength energy measured in micrometers that is reflected, scattered, transmitted, and/or absorbed by the first few layers of leaves and stems of a healthy vegetation canopy. We typically get little information about the internal characteristics of the canopy, much less information about the surface soil characteristics lying below the canopy. Conversely, active microwave energy can penetrate the canopy to varying depths depending upon the frequency, polarization, and incident angle of the radar system. Microwave energy responds to objects in the plant's structure that are measured in centimeters and even decimeters. It is useful to identify the relationship between the canopy components and how they influence the radar backscattering.

If a radar sends a pulse of vertically or horizontally polarized microwave energy toward a stand of trees, it interacts with the components present and scatters some of the energy back toward the sensor. The amount of energy received is proportional to the nature of the energy sent (its frequency and polarization) and is dependent upon whether or not the canopy components depolarize the signal, how far the signal penetrates into the canopy, and whether it eventually interacts with the ground soil surface.

Penetration Depth and Polarization

Like-polarization backscatter toward the sensor results from single reflections from canopy components such as the leaves, stems, branches, and trunk. These returns are generally very strong and are recorded as bright signals in like-polarized radar imagery (HH or VV). This is often called canopy *surface scattering*. Conversely, if the energy is scattered multiple times within a diffuse volume such as a stand of pine trees (i.e., from a needle, to a stem, to the trunk, to a needle), the energy may become depolarized. This is often called *volume scattering*. A radar can measure the amount of depolarized volume scattering that takes place. For example, it is possible to configure a radar to send a vertically polarized pulse of energy. Some of this energy becomes depolarized in the canopy and exits toward the sensor in the horizontal domain. The depolarized energy may then be recorded by the sensor in VH mode – vertical send and horizontal receive.

Kasischke and Bourgeau-Chavez (1997) provide insight as to how the radar backscattering coefficient, σ°, from both woody (forested) and non-woody (e.g., brush, scrub, crops) environments is produced when the terrain is impacted by microwave energy.

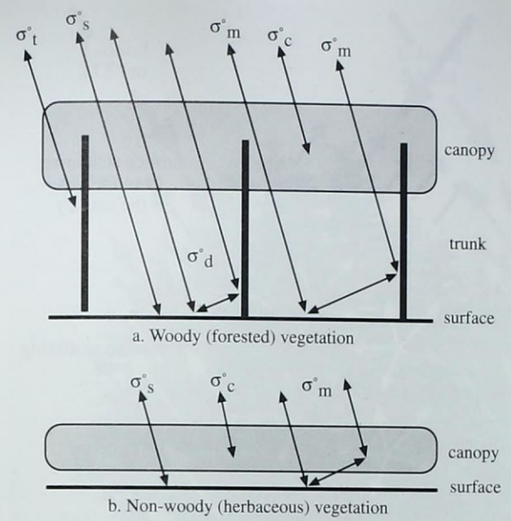

Figure 9-21 The major sources of scattering from a) woody and b) herbaceous vegetation canopies where σ°_c is the backscatter coefficient of the crown layer of smaller woody branches and foliage (i.e., surface scattering), σ°_m is the multiple-path scattering between the ground and canopy layer, σ°_t is direct scattering from the tree trunks, σ°_s is direct surface backscatter from the ground, and σ°_d is the double-bounce scattering between the tree trunks and ground (courtesy of American Society for Photogrammetry & Remote Sensing; Kasischke and Bourgeau-Chavez, 1997).

To understand radar-scattering from complex vegetation covers, it is necessary to think in terms of the different canopy layers affecting the radar signature. For wetlands containing shrubs and trees, there are three distinct layers to consider, as shown in Figure 9-21a: 1) a canopy layer that consists of small branches and foliage (leaves), 2) a trunk layer that consists of large branches and trunks or boles, and 3) a surface layer that may or may not be covered by water if wetland is present. For wetlands that do not contain woody plants, a simple two-layer model can be used (Figure 9-21b): 1) a canopy layer consisting of herbaceous vegetation, and 2) a surface layer that may be covered by water or soil. The backscattering coefficient exiting a woody vegetation canopy toward the radar system is σ°_w and can be expressed as (Wang et al., 1995; Dobson et al., 1995; Kasischke and Bourgeau-Chavez; 1997):

$$\sigma^\circ_w = \sigma^\circ_c + \tau_c^2\tau_t^2(\sigma^\circ_m + \sigma^\circ_t\,\sigma^\circ_s + \sigma^\circ_d) \qquad (9\text{-}24)$$

where

- σ°_c is the backscatter coefficient of the canopy layer of smaller woody branches and foliage (i.e., surface scattering),
- τ_c is the transmission coefficient of the vegetation canopy,
- τ_t is the transmission coefficient of the trunk layer,
- σ°_m is the multiple-path scattering between the ground and canopy layer,
- σ°_t is direct scattering from the tree trunks,
- σ°_s is direct surface backscatter from the ground, and
- σ°_d is the double-bounce scattering between the trunks and the ground.

By eliminating all terms associated with the trunk layer, it is possible to determine the total radar-scattering coefficient from terrain with non-woody, herbaceous vegetation, σ°_h:

$$\sigma^\circ_h = \sigma^\circ_c + \tau_c^2(\sigma^\circ_s + \sigma^\circ_m)\,. \qquad (9\text{-}25)$$

The terms in Equations 9-24 and 9-25 are dependent on 1) the type of vegetation present (which has an impact on surface roughness), 2) the wavelength and polarization of the incident microwave energy, 3) the dielectric constant of the vegetation, and 4) the dielectric constant of the ground surface. The scattering and attenuation in the equations are all directly proportional to the dielectric constant. Live vegetation, with a higher water content (turgidity) has a higher dielectric constant than drier or dead vegetation. The presence of dew or moisture acts to increase the dielectric constant of vegetated surfaces (Kasischke and Bourgeau-Chavez, 1997). Often, the primary quantity governing the attenuation coefficient of a vegetation canopy is the water content per unit volume, not necessarily the actual structure and geometry of the leaves, stems, and trunk of the plants.

The condition of the ground layer is also very important in microwave scattering from vegetation surfaces. There are two properties of this layer that are important, including: 1) the micro- and mesoscale surface roughness (relative to the radar wavelength previously discussed), and 2) the reflection coefficient. In general, a greater surface roughness 1) increases the amount of microwave energy backscattered (increasing σ°_s), and 2) decreases the amount of energy scattered in the forward direction (decreasing σ°_m and σ°_d). The reflection coefficient is dependent on the dielectric constant

(or conductivity) of the ground layer. A dry ground layer has a low dielectric constant and therefore has a low reflection coefficient. As soil moisture increases, so does the dielectric constant and, hence, the reflection coefficient. Given a constant surface roughness, as the soil dielectric constant increases, so does both the amount of backscattered and forward scattered microwave energy (resulting in increases in σ°_m, σ°_s, and σ°_d).

If there is a layer of water over the ground surface of a vegetated landscape such as in wetland environments, two things happen: 1) it eliminates any surface roughness, and 2) it significantly increases the reflection coefficient. In terms of microwave scattering, the elimination of any surface roughness means that all the energy is forward scattered, eliminating the surface backscattering term (σ°_s) in the equations; and, the increased forward scattering and higher reflection coefficient lead to significant increases in the ground-trunk and ground-canopy interaction terms σ°_d and σ°_m respectively (Kasischke and Bourgeau-Chavez, 1997).

Penetration Depth and Frequency

The longer the microwave wavelength, the greater the penetration into the plant canopy. For example, Figure 9-22 depicts the response of a hypothetical pine forest to microwave energy. Surface scattering takes place at the top of the canopy as the energy interacts with the leaves (or needles) and stems. Volume scattering by the leaves, stems, branches, and trunk takes place throughout the stand, and surface scattering can occur again at the soil surface. A comparison of the response of X-, C-, and L-band microwave energy incident to the same canopy is presented in Figure 9-23a–c. The shorter wavelength X-band (3 cm) energy is attenuated most by surface scattering at the top of the canopy by foliage and small branches. The C-band (5.8 cm) energy experiences surface scattering at the top of the canopy as well as some volume scattering in the heart of the stand. Little energy reaches the ground. L-band (23.5 cm) microwave energy penetrates farther into the canopy, where volume scattering among the leaves, stems, branches, and trunk cause the beam to become depolarized. Also, numerous pulses may be transmitted to the ground, where surface scattering from the soil-vegetation boundary layer may take place. Longer P-band radar (not shown) would afford the greatest penetration through the vegetation and mainly reflect off large stems and the soil surface (Waring et al., 1995).

Radar Backscatter and Biomass

Radar backscatter increases approximately linearly with increasing biomass until it saturates at a biomass level that depends on the radar frequency. For example, Dobson et al. (1992) found that the biomass saturation level was about 200 tons/ha of Loblolly pine using P-band and 100 tons/ha at L-band, and that the C-band backscattering coefficient showed much less sensitivity to total aboveground biomass. Wang et al. (1994) evaluated Loblolly pine using ERS-1 SAR backscatter data. They also found that the C-band functioned poorly due to its high sensitivity to soil moisture and the steep local incident angle of the sensor (23°). Generally, backscatter at lower frequencies (P- and L-bands) is dominated by scattering processes involving the major woody biomass components (trunks and branches), while scattering at high frequencies (C- and X-bands) is dominated by scattering processes in the top crown layer of branches and foliage. Radar canopy measurements have also been found to be correlated with leaf-area-index (LAI) measurements (Franklin et al., 1994).

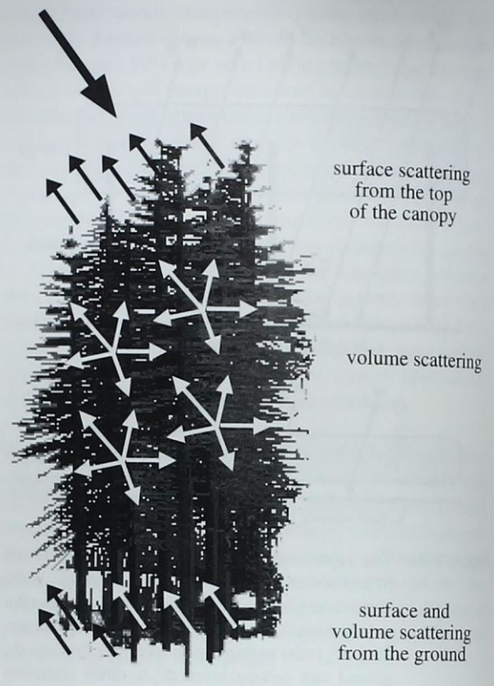

Figure 9-22 The types of active microwave surface and volume scattering that might take place in a hypothetical pine forest stand (after Carver, 1988).

Some other general observations about SAR vegetation interpretation include:

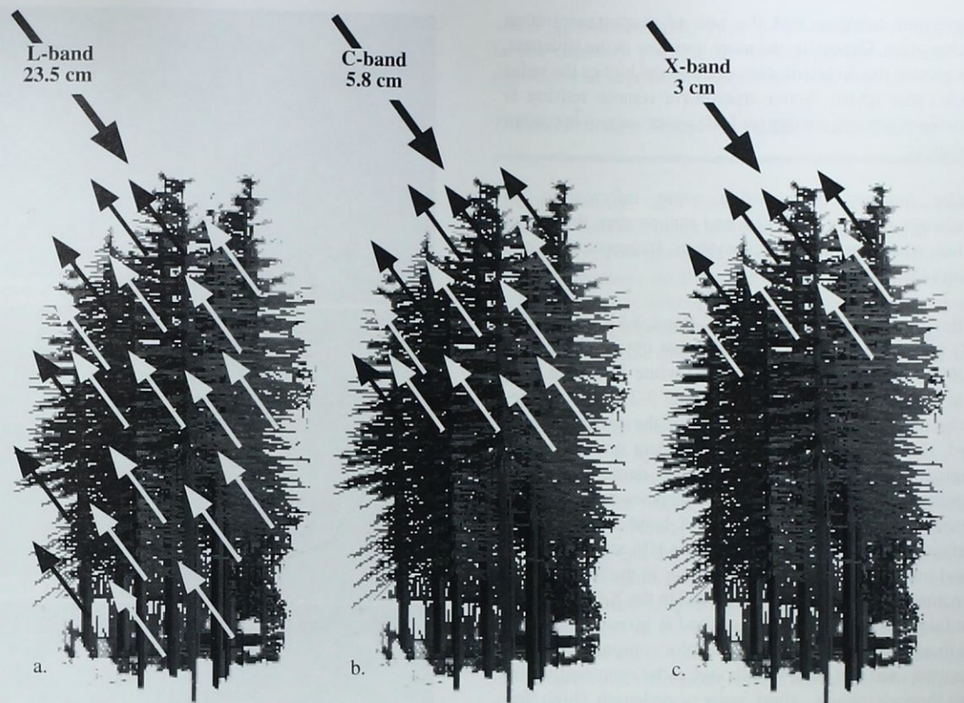

Figure 9-23 Theoretical response of a pine forest stand to X-, C-, and L-band microwave energy. The shorter the wavelength, the greater the contribution from *surface scattering*. The longer the wavelength, the greater the penetration into the material and the greater the *volume scattering*.

- Vertically polarized energy is highly attenuated by the vertically oriented canopy components (leaves, stems, branches, and trunk) while horizontally polarized energy is not.

- The brighter the return on like-polarized radar images (HH or VV), the greater the contribution from surface scattering.

- The brighter the return on cross-polarized images (HV or VH), the greater the contribution from volume (internal canopy) scattering (Avery and Berlin, 1992).

- When the radar wavelength is approximately the same size as the canopy components (e.g., C- or X-band), substantial surface and volume scattering will take place and little energy may reach the ground. Consequently, shorter wavelength radars (2 – 6 cm) may be preferred when monitoring crop canopies and tree leaves. Longer wavelength radars (9 – 30 cm) exhibit substantial volume scattering as incident energy interacts with larger trunk and branch components. Considerable surface scattering from the underlying soil may also occur which can cause confusion.

- Cross-polarized images (HV or VH) are less sensitive to slope variations. This suggests vegetation monitoring in mountainous areas may best be performed using cross-polarization techniques. Also, the same row crop planted in different directions can produce like-polarized images that are difficult to interpret. This ambiguity may be reduced when cross-polarized images are available in addition to like-polarized images.

- One of the key variables necessary to model the hydrological cycle is how much water is being stored in

vegetation canopies and the rate of evapotranspiration taking place. Generally, the more moisture in the structure, the greater the dielectric constant and the higher the radar backscatter return. Active microwave remote sensing is capable of sensing canopy (or leaf) water content in certain instances.

- Radar imagery can provide some information on landscape-ecology patch size and canopy gaps that are of value when monitoring ecosystem fragmentation and health (Sun and Ranson, 1995).

Shuttle Imaging Radar C- and X-Band SAR (SIR-C/X-SAR) images of the Amazon rain forest obtained on April 10, 1994, are displayed in black-and-white in Figure 9-24 and as a color composite in Color Plate 9-2. These images may be used to demonstrate several of the concepts mentioned. First, the multifrequency radar data reveals rapidly changing land-use patterns, and it also demonstrates the capability of the different radar frequencies to detect and penetrate heavy rainstorms. The top X-band image has VV polarization, the center C-band image is HV, and the bottom L-band image is HV. A heavy downpour in the lower center of the image appears as a black "cloud" in the X-band image, more faintly in the C-band image, and is invisible in the L-band image. When combined in the color composite, the rain cell appears red and yellow. Although radar can usually penetrate through clouds, short radar wavelength (high frequency), such as X- and C-band, can be changed by unusually heavy rain cells. L-band, at 23.5 cm (9 in.) wavelength, is relatively unaffected by such rain cells. Such information has been used to estimate rainfall rates (NASA JPL, 1996). Of course, there is very little backscatter from the river in all three radar images, causing it to appear black.

The area shown is in the state of Rondonia, in western Brazil. The pink areas in the color composite are pristine tropical rain forests, and the blue and green patches are areas where the forest has been cleared for agriculture. Radar imaging can be used to monitor not only the rain forest modification but also the rates of recovery of abandoned fields. Inspection of the black-and-white images reveals that as the wavelength of the radar progresses from X- to C- to L-band, it becomes easier to discriminate cleared land from rain forest. In the L-band black-and-white image, the cleared land appears relatively dark while the rainforest appears very bright. Evidently, the cleared land contains sufficient scatterers to cause it to appear bright at X- and C-band frequencies, while at L-band frequencies the incident energy to the cleared fields is reflected away from the radar receiver. The rain forest appears relatively bright in all images because of

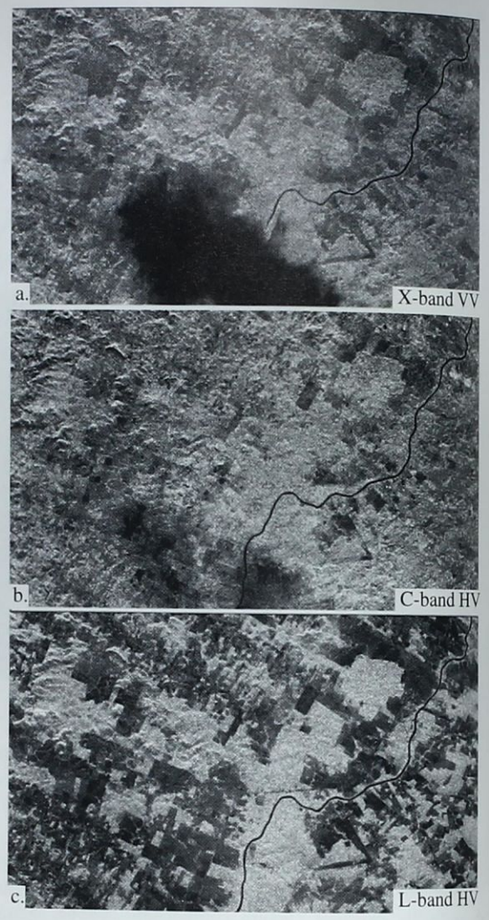

Figure 9-24 SIR-C/X-SAR images of a portion of Rondonia, Brazil, obtained on April 10, 1994. a) X-band image with VV polarization. b) C-band image is HV. c) L-band image is HV. A heavy rain in the lower center of the image appears as a black "cloud" in the X-band image, more faintly in the C-band image, and is invisible in the L-band image. L-band, at 24 cm (9 in) wavelength, is relatively unaffected by such rain cells. Also, the L-band image differentiates the pristine rain forest (bright) from the darker clear-cut areas because it penetrates farther into the canopy, experiencing greater volume scattering. Water, of course, is dark in all three bands. A color composite of the three images is found in Color Plate 9-2 (courtesy NASA Jet Propulsion Lab).

1) the tremendous number of leaves, branches, stems, and trunks that can contribute to canopy surface scattering and volume scattering within the canopy (L-band penetrates the greatest distance into the canopy and is brighter), and 2) there is a high moisture content in the rain forest canopy, further increasing the amount of backscatter present in all three bands (NASA JPL, 1996).

Water Response to Microwave Energy

Flooding occurs periodically in many areas, and cloud cover obscures the collection of data using optical and thermal sensors. Fortunately, the smooth surface of standing water reflects almost all the incident microwave radiation away from the sensor (unless there is a strong wind with lots of chop, which can cause confusion), resulting in lower backscatter than a dry surface. When standing water is present under vegetation, a unique corner-reflection backscatter interaction between surface water and tree stems results in an extremely high backscatter and allows inundation to be clearly mapped (Hess et al., 1990; Waring et al., 1995). Ford et al. (1986) demonstrated how wetlands along the Savannah River appeared especially bright compared to standing water and other upland land cover such as Loblolly pine, due to this corner-reflector condition between the water and cypress-tupelo tree trunks.

Assessing Soil Moisture

L-band radar penetrates into bare, damp, smooth soil to a maximal depth of approximately 10 cm. Shorter wavelengths penetrate to only 1 – 3 cm. In agricultural fields that have smooth soil surfaces and biomass of less than 1 mg/ha, moisture content of surface layers can be fairly accurately determined (Wang et al., 1994). Once vegetation biomass exceeds a certain limit, the ability of radar to sense surface soil-water conditions decreases rapidly (Waring et al., 1995). Under a dense forest canopy, the amount of moisture held in the leaves is so large that it interferes with any direct assessment of soil-water status (Jackson and Schmugge, 1991).

Thus, the presence of vegetation over the soil surface can add considerable complexity to measuring soil moisture using microwave remote sensing techniques. Because the vegetation's transmissivity decreases with increasing microwave frequency, it is best to use the longest wavelength available for soil moisture mapping (Dobson and Ulaby, 1998). This would be P-band ($\lambda = 68$ cm) for aircraft SARs and L-band ($\lambda = 23$ cm) for satellite SARs. If the vegetation biomass is < 0.5 kg/m^2, the effect of the vegetation backscatter may be ignored for like-polarized L-band data, i.e., σ°_{VV} and σ°_{HH}. Unfortunately, when the biomass is > 0.5 kg/m^2, it is not currently possible to disentangle the separate soil moisture and vegetation backscatter contributions.

Urban Structure Response to Microwave Energy

Urban buildings, cars, fences, bridges, etc., act as corner reflectors that send much of the incident energy back toward the antenna. This generally results in bright signatures for urban phenomena on the radar image. Unfortunately, this plethora of bright returns is often confusing in radar images of urban areas especially when 1) the cardinal effect takes place, and/or 2) the imagery is of relatively low spatial resolution.

A SIR-C/X-SAR image of Los Angeles, CA, is found in Figure 9-25. It has approximately 30 x 30 m resolution. The radar look-direction is from the top to the bottom of the image. Only the major terrain features can be resolved, including the freeways, major urban development, the Pacific Ocean, and the mountainous terrain. In general, it is not possible to distinguish between commercial and residential communities. Interestingly, there are some very bright polygonal areas in the image. These are produced by the radar *cardinal effect*. Early in radar remote sensing research it was noted that reflections from urban areas, often laid out according to the cardinal points of the compass, caused significantly larger returns when the linear features were illuminated by the radar energy at an angle orthogonal (perpendicular) to their orientation (Raney, 1998). For example, the residential communities of San Fernando and Santa Monica are for all practical purposes similar in nature to other residential communities in their vicinity (Figure 9-25). However, due to the cardinal effect caused by their unique orientation relative to the SIR-C sensor system at the time of data collection, they appear in the radar image to contain land-cover that is dramatically different than the other residential communities found throughout the Los Angeles basin.

It has been demonstrated repeatedly that two identical tracts of urban land (e.g., two single-family housing tracts) built at the same time, with the same lot size, and using the same materials will appear dramatically different from one another on radar imagery if one is laid out in a different orientation than the other, e.g., one is laid out with streets trending northeast and one is laid out with streets trending due north. Similarly, the regular spacing of agricultural row crops can produce a similar effect. Also, the same parcel of urban land may appear quite different on radar imagery acquired on two different dates if practically any of the sys-

SIR-C/X-SAR Image of Greater Los Angeles, California

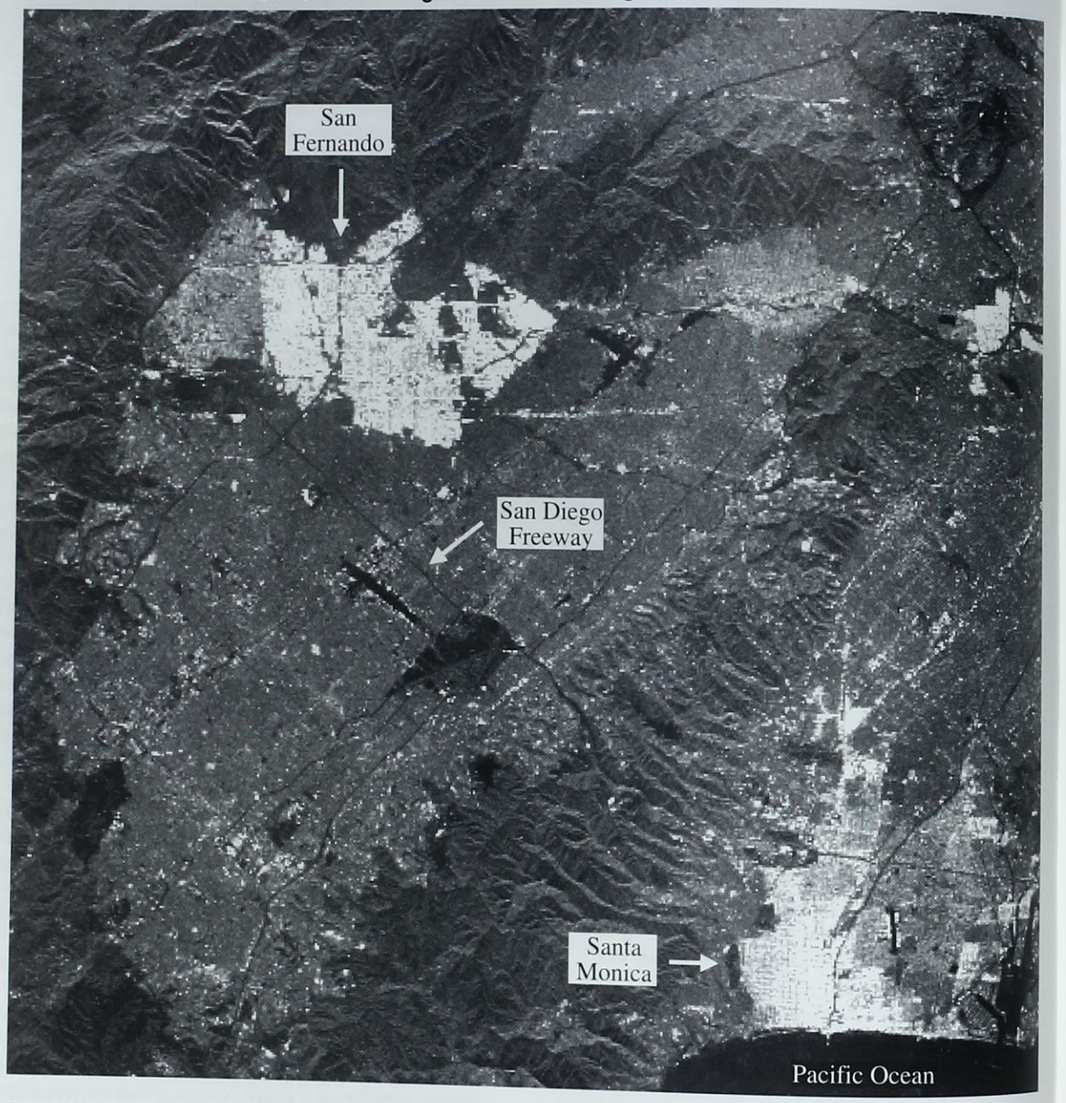

Figure 9-25 The cardinal effect is responsible for the pronounced bright signature of portions of Santa Monica and San Fernando in this SIR-C/X-SAR image of the Los Angeles basin obtained on October 3, 1994. The look direction is from the top to the bottom of the image (courtesy NASA Jet Propulsion Laboratory).

tem parameters are changed, especially look direction. This plays havoc when attempting to perform digital change detection using radar imagery.

RADARSAT, JERS-1, and ERS-1,2, with their relatively coarse spatial resolutions (Table 9-1) may be of value for obtaining general Level I land-cover and land-use information. When attempting to extract Level II and III urban land-cover and land-use information, optical remote sensor data is usually superior. However, if high spatial resolution radar is available, then detailed urban information may be extracted. For example, a photograph and a radar image of the Pentagon are found in Figure 9-26. Henderson and Xia (1998) provide examples of how settlement patterns and socioeconomic information such as population estimates may be extracted from radar data.

SAR Remote Sensing from Space

The following sections summarize the characteristics of the major satellite SAR sensor systems.

Seasat

Seasat was launched by NASA on June 26, 1978, and functioned for 105 days. It carried an L-band (23.5 cm) active microwave SAR at an altitude of 800 km. The antenna was 10.7 x 2.16 m in dimension. It collected HH-polarized data at an incident angle of 23°. It had a range resolution of 25 m and an azimuth resolution of 25 m. The swath width was 100 km. The data were processed with "4 looks." Seasat had an orbital repeat cycle of 17 days. The data were processed originally optically and then digitally.

Shuttle Imaging Radar SIR-A, SIR-B, SIR-C

Several very important scientific radar instruments have been carried aboard NASA's Space Shuttle and operated for a number of days before returning to Earth. SIR-A and SIR-B were launched on November 12, 1981, and October 5, 1984, respectively, and were in orbit for 2.5 and 8 days. Both payloads consisted of an L-band (23.5 cm) SAR.

SIR-A had a 9.4 x 2.16 m antenna with HH polarization. The incident angle was 50°. The sensor had a range and azimuth resolution of 40 m with 6 looks. The swath width was 50 km. The Shuttle was in orbit at 260 km above the Earth. The data were processed optically.

SIR-B had a 10.7 x 2.16 m antenna with HH polarization. It had an incident angle of 15 – 64°. Its azimuth resolution was 17 – 58 m and its range resolution was 25 m with 4 looks. The swath width was 10 – 60 km. It operated at 225 and 350 km above the Earth. The data were processed both optically and digitally.

SIR-C was a significant breakthrough in radar remote sensing. It was a joint project between the United States (NASA JPL) and a consortium of European groups. SIR-C carried aloft a three frequency SAR: X-band (3 cm), C-band (5.8 cm), and L-band (23.5 cm). The three antennas were placed on a common platform in the Shuttle bay. The L- and C-bands had quad polarization (i.e., HH, HV, VV, and VH) while the X-band had VV polarization. The incident angle was from 15 – 55°. The range resolution was 10 - 30 m, and the azimuth resolution was 30 m with approximately 4 looks. The swath width was 15 – 90 km. It was flown at 225 km above the Earth. The data were processed digitally. *This was the first true multifrequency, multipolarization space-borne SAR.* Data from all three bands are excellent and widely available through JPL and other locations. Several examples of SIR-C data are found in this chapter and in the color plate section.

RADARSAT

RADARSAT was launched by the Canadian government on November 4, 1995, into a near-polar, Sun-synchronous orbit 798 km above the Earth. It has a dawn-to-dusk orbit, meaning it crosses the equator at dawn and dusk (approximately 6:00 a.m. and p.m. local time) and is rarely in eclipse or darkness. The orbital inclination is 98.6° with a period of 100.7 minutes and 14 orbits per day. It has a single C-band (5.6 cm) active microwave sensor that transmits at 5.3 GHz frequency at a pulse length of 42.0 μs. The antenna size is 15 x 1.5 m. Its polarization is horizontal-send and horizontal-receive (HH) (Raney, 1991).

Unlike many of the other sensors to be discussed, RADARSAT provides a range of spatial resolutions and geographic coverages. There are seven image sizes, termed *beam modes,* summarized in Figure 9-27 and Table 9-5. Each beam mode is defined by the geographic area it covers and the spatial resolution. The beam modes range from *Fine,* which covers a 50 x 50 km area and has a 10 x 10 m spatial resolution, to *ScanSAR Wide,* which covers a 500 x 500 km area at 100 x 100 m spatial resolution.

RADARSAT obtains data using a range of incident angles from less than 20° (steep angle) to almost 60° (shallow

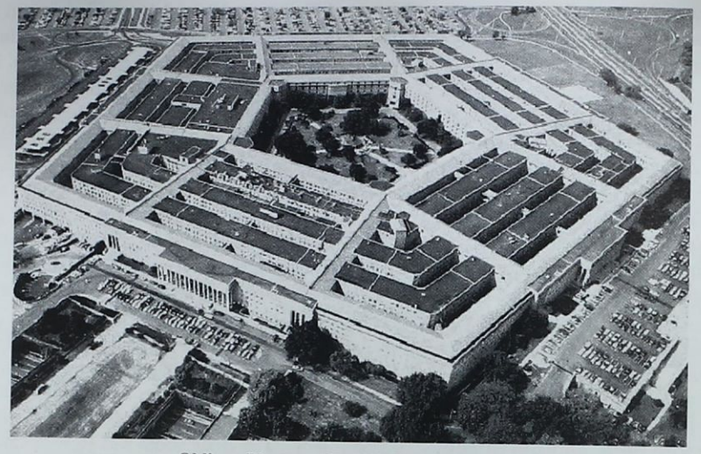

a. Oblique Photograph of the Pentagon

b. Radar Image of the Pentagon

Figure 9-26 a) Low-oblique aerial photograph of the Pentagon in Washington, DC. b) Synthetic aperture radar image of the Pentagon (courtesy of Federation of American Scientists).

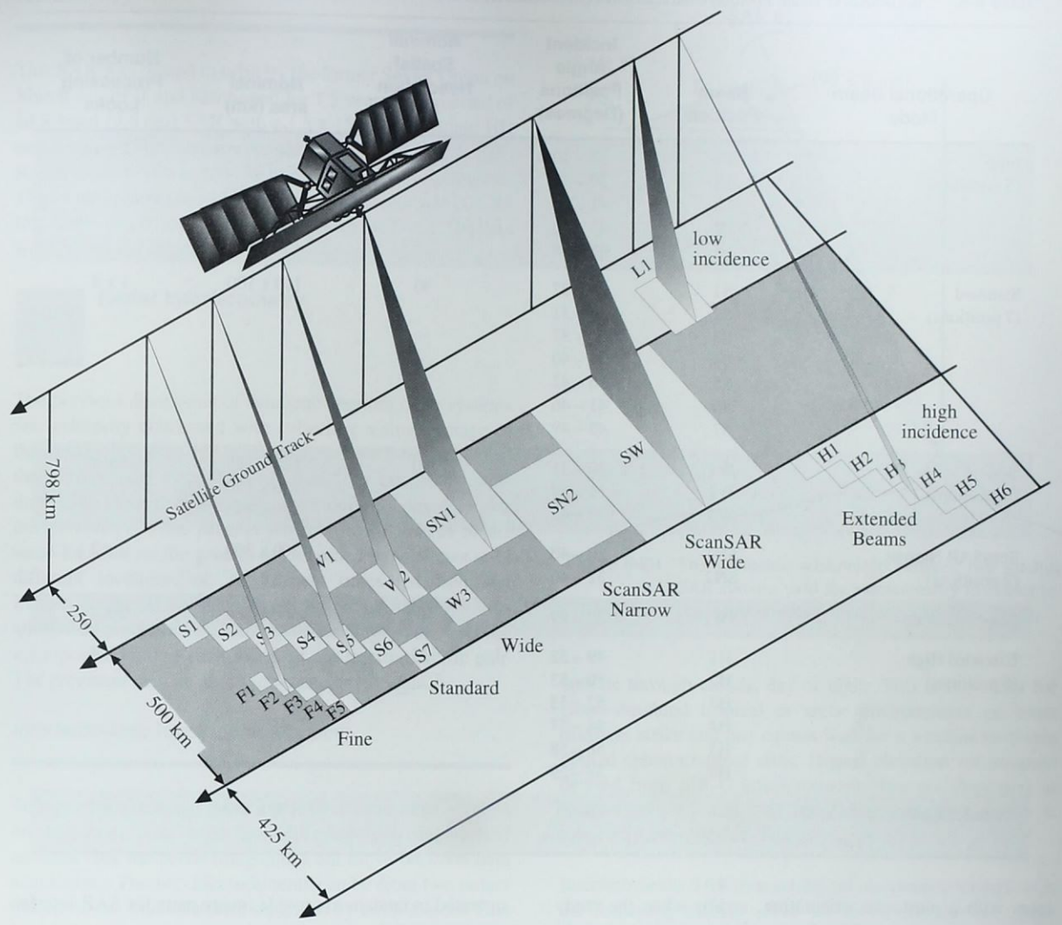

Figure 9-27 The beam modes and incident angle options for acquiring RADARSAT data. The size of the footprints provide information on the spatial resolution. Refer to Table 9-5 for specifications (after RADARSAT, International, Inc.).

angle). Within each beam mode, a number of incident angle positions are available (Figure 9-27 and Table 9-5). These are called *beam positions*. For example, Standard beam mode, which covers a 100 x 100 km area, has seven beam positions. By specifying a beam position, one of seven 100 x 100 km images within a 500 km accessible swath will be collected. Factors influencing the choice of beam mode include the sensitivity of the application to incident angle, type of terrain, stereo requirements, spatial resolution desired, and how often coverage of the area is required.

RADARSAT's orbit has a 24-day cycle, meaning it returns to the same location every 24 days. However, it can be pointed to provide a more frequent revisit cycle. The user also has the option of collecting imagery based on two different look directions. As RADARSAT descends from the North Pole (a descending orbital pass), it views the Earth in a westerly direction. As it ascends from the South Pole (an ascending orbital pass) it views the Earth in an easterly direction. This can be very useful when working in areas with high relief, when we are interested in highlighting fea-

Table 9-5. RADARSAT Beam Position Characteristics (RADARSAT, 1998)

Operational Beam Mode	Beam Position	Incident Angle Positions (Degrees)	Nominal Spatial Resolution (m)	Nominal area (km)	Number of Processing Looks
Fine (5 positions)	F1	37 – 40	10	50 x 50	1 x 1
	F2	39 – 42			
	F3	41 – 44			
	F4	43 – 46			
	F5	45 – 48			
Standard (7 positions)	S1	20 – 27	30	100 x 100	1 x 4
	S2	24 – 31			
	S3	30 – 37			
	S4	34 – 40			
	S5	36 – 42			
	S6	41 – 46			
	S7	45 – 49			
Wide (3 positions)	W1	20 – 31	30	165 x 165	1 x 4
	W2	31 – 39		150 x 150	
	W3	39 – 45		130 x 130	
ScanSAR Narrow (2 positions)	SN1	20 – 40	50	300 x 300	2 x 2
	SN2	31 – 46			
ScanSAR Wide	SW1	20 – 49	100	500 x 500	2 x 4
Extended High (6 positions)	H1	49 – 52	25	75 x 75	1 x 4
	H2	50 – 53			
	H3	52 – 55			
	H4	54 – 57			
	H5	56 – 58			
	H6	57 – 59			
Extended Low	L1	10-23	35	170 x 170	1 x 4

tures with a particular orientation, and/or when the study requires imagery acquired in the early morning or early evening. RADARSAT-2 will be launched in the early twenty-first century.

European Space Agency ERS-1

The European Space Agency launched the ERS-1 on July 16, 1991. It has a C-band (5.6 cm) SAR with a 10 x 1 m antenna and VV polarization. It functions with an incident angle of 23°. The range resolution is 26 m and the azimuth resolution is 30 m with 6 looks. It has a swath width of 100 km. It is in orbit approximately 785 km above the Earth. The data are processed digitally. An identical ERS-2 was launched in 1995. ERS-1 and ERS-2 have on occasion been operated in tandem to provide image pairs for SAR interferometry research.

JERS-1

The National Space Development Agency (NASDA) of Japan launched the Japanese Earth Resource Satellite (JERS-1) on February 11,1992. It is very similar to the original Seasat. It has an L-band (23.5 cm) SAR with an 11.9 x 2.4 m antenna and HH polarization. The incident angle is 39°. Range and azimuth resolution are both 18 m with 3 looks. The swath width is 75 km. The SAR orbits at approximately 568 km above the Earth. The data are processed digitally. JERS-1 operation was terminated on October 12, 1998.

Almaz-1

This SAR was placed in orbit by the former Soviet Union on March 31, 1991 and functioned for 1.5 years. It consisted of an S-band (9.6 cm) SAR with a 1.5 x 15 m antenna and HH polarization. The incident angle ranged from 30 – 60°. Range resolution was 15 – 30 m and azimuth resolution was 15 m with greater than 4 looks. The swath width was 20 – 45 km. It was placed in a 300 km orbit above the Earth. The data were processed digitally.

Radar Interferometry

The previous discussion of synthetic aperture radar systems was primarily concerned with collecting a single image of the terrain. It is possible to acquire multiple SAR images of the terrain from aircraft or spacecraft to extract valuable three-dimensional and velocity information. *Imaging radar interferometry* is the process whereby radar images of the same location on the ground are recorded by antennas at 1) different locations, or 2) different times (Madsen and Zebker, 1998). Analysis of the resulting two interferograms allow very precise measurements of the range to any specific x,y,z point found in each image of the interferometric pair. The precision may be at the sub-wavelength scale.

Interferometric Topographic Mapping

Topographic mapping based on SAR interferometry relies on acquiring data from two different look angles and assumes that the scene imaged did not move between data acquisitions.The two measurements can be from two radars placed on the same platform separated by a few meters. This is called *single-pass interferometry.* The first single-pass interferometric SAR is the Shuttle Radar Topography Mission (SRTM) to be launched early in the twenty-first century. It has a C-band and an X-band antenna separated by 60 m. Interferometry may also be conducted using a single radar that obtains two measurements on different orbital tracks that are closely spaced but a day or so longer apart. This is the methodology used for the SIR-C and ERS-1,2 interferometry and is called *multiple-pass* or repeat pass interferometry.

Interferometric SAR data can provide extremely high precision topographic information (x,y,z) that is just as accurate as digital elevation models derived using traditional optical photogrammetric techniques. However, interferometry can operate through clouds, day or night. This is important for cloud-shrouded tropical or arctic environments or when disasters strike and one cannot wait for a window to obtain optical (photographic) data. Digital elevation information derived from SIR-C interferometric data are displayed in Color Plates 9-3 and 9-4. The cartographic community is especially interested in interferometric SAR.

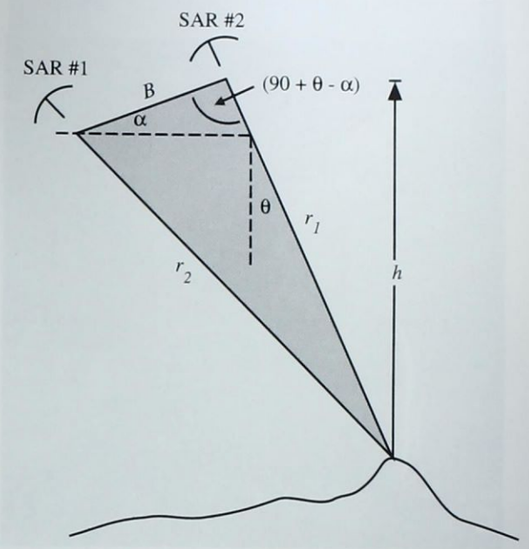

Figure 9-28 The geometric relationship between two satellite SAR systems used for interferometry to extract topographic information (after NASA JPL, 1999b).

Interferometric SAR obtains digital elevation information in the following manner (JPL, 1999b). First, the two radar images must be precisely registered. Then their geometry is such that the two radars and any object on the ground form a triangle (Figure 9-28). If we know the distance (range) from each radar to the object on the ground (r_1 and r_2), the distance between the two radars (the baseline B) and the angle of that baseline, α (with respect to the horizontal), we can use trigonometry (the cosine rule) to calculate the height, h, of one of the radars above the position of the object on the ground. From Figure 9-28 we know that:

$$h = r_1 \cos\theta \tag{9-26}$$

and by the cosine rule,

$$(r_2)^2 = (r_1)^2 + B^2 - 2r_1 B\cos(90 + \theta - \alpha) \tag{9-27}$$

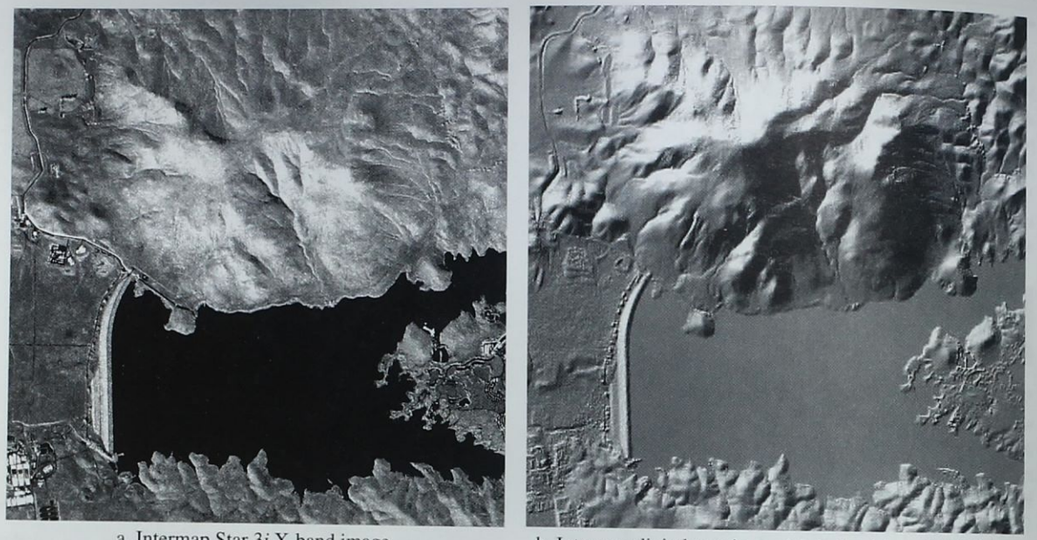

a. Intermap Star 3*i* X-band image

b. Intermap digital terrain model derived from IFSAR data

Figure 9-29 a) Intermap X-band Star 3*i* orthorectified image of Bachelor Mountain, CA. b) Digital elevation model of the same area derived using interferometric synthetic aperture radar (IFSAR) techniques (orthorectified imagery and Global Terrain Digital Elevation Model provided by Intermap Technologies, Inc.).

which is the same as:

$$(r_2)^2 = (r_1)^2 + B^2 - 2r_1 B\sin(\theta - \alpha). \qquad (9\text{-}28)$$

We solve for θ, then for h (using $h = r_1 \cos\theta$). This calculation is repeated for every point on the ground within the image. If we determine the precise height of one of the radars above sea level, we can produce a map of the surface heights. It turns out that we can only precisely measure the relative distance ($r_2 - r_1$) from the phase difference between each pair of radar measurements. This relative distance can be related to the height, h, after some additional algebra (SIR-CED home page; JPL, 1999b).

The Shuttle Radar Topography Mission (SRTM) will use C-band and X-band interferometric synthetic aperture radars (IFSARS) to acquire topographic data over 80 percent of the Earth's land mass (between 60° N and 56° S) during an 11 day mission. The topographic maps produced will meet Interferometric Terrain Height Data (ITHD-2) specifications. Thus, the first worldwide collection of digital elevation data will be acquired using interferometry, not photogrammetry. The interferometer pairs will also be of significant value for many Earth resource applications.

Private commercial companies also provide interferometric synthetic aperture radar (IFSAR) data. One of the most widely used is the Intermap X-band Star 3*i* system which generates high quality 3 x 3 m X-band microwave imagery plus a detailed digital elevation model of the terrain. A good example is shown in Figure 9-29 with the X-band image of Bachelor Mountain, CA, on the left and the digital elevation model on the right. Of course, the radar image and the DEM are registered. Such data are very valuable for land-use and land-cover analysis as well as watershed hydrologic studies.

Interferometric Velocity Mapping

If the look angles of multiple data acquisitions are held constant, there is no sensitivity to topography and the interferometry can be used to extract information about things that have changed in the scene. Quantitative information about the velocity of objects that moved between the two observations may be made. Interferometry has been successfully applied to measuring movement along fault lines, measuring seismic displacement due to earthquakes, mapping glacier velocity, monitoring ocean currents, and measuring wave spectra. In addition, interferometry can be used to determine if man-made objects in the scene have moved. This is very powerful for change detection purposes.

Passive Microwave Remote Sensing

There is a growing interest in the measurement of passive microwave energy to monitor some of the more important global hydrologic variables such as soil moisture, precipitation, ice water content, and sea-surface temperature. In fact, several sensors onboard Earth Observing System PM-1 will include specialized passive microwave radiometers.

As discussed in Chapter 2, the Earth approximates a 300 K blackbody with a dominant wavelength of approximately 9.7 μm. While the dominant wavelength may be 9.7 μm, a continuum of energy is emitted from the Earth and the atmosphere. In fact, the Earth passively emits a steady stream of microwave energy. The only difference is that 1) the Earth's materials do not emit a tremendous amount of passive microwave energy, and 2) what energy it does emit is relatively weak in intensity due to its long wavelength. Nevertheless, a suite of radiometers have been developed that can record subtle, passive microwave energy. The instruments measure the *brightness temperature* of the terrain or the atmosphere and its constituents (Engman and Gurney, 1991).

Passive Microwave Radiometers

Passive microwave remote sensing devices may be 1) profiling radiometers, or 2) scanning radiometers. A profiling radiometer simply stares at the terrain directly beneath the craft at nadir (or off-nadir if desired) and records the radiance from within the instantaneous field of view of the sensor. The output is a profile of the microwave brightness temperature recorded as the aircraft or spacecraft moves forward. A scanning microwave radiometer is much like the scanning thermal infrared radiometer discussed in Chapter 8. It collects data across-track as the craft moves forward. The result is a matrix of brightness temperature values that can be used to construct a passive microwave image.

Passive microwave radiometers generally record energy in the region between 0.15 and 30 cm (between 1 and 200 GHz), well beyond the thermal infrared region (3 – 14 μm). The microwave frequencies most commonly used are centered at 1, 4, 6, 10, 18, 21, 37, 50, 85, 157, and 183 GHz. This means that it is theoretically possible to acquire multi-spectral passive microwave imagery. The actual bandwidths (range of frequencies) recorded are usually fairly broad so that enough passive microwave energy is available to be recorded by the antenna. Similarly, the spatial resolution of passive microwave radiometers is usually large so that sufficient energy is collected within the instantaneous field of view to be recorded by the antenna. Aircraft sensors flying closer to the ground may have spatial resolutions measured in meters while most satellite passive microwave scanning radiometers have a spatial resolution measured in kilometers. The sensor is actually a large antenna sensitive to passive microwave energy.

Figure 9-30 SSM/I passive microwave radiometer image of the Amazon Basin obtained at a frequency of 85 GHz with vertical polarization (courtesy DMSP).

Special Sensor Microwave/Imager (SSM/I)

One of the first passive microwave sensors was the Special Sensor Microwave/Imager (SSM/I) onboard the Defense Meteorological Satellite Program (DMSP) satellites since 1987. Fortunately, the Department of Defense releases the data to the scientific community (Figure 9-30). The SSM/I is a four-frequency, linearly polarized passive microwave radiometric system that measures atmospheric, ocean and terrain microwave brightness temperatures at 19.35, 22.23, 37.0, and 85.5 GHz. The SSM/I rotates continuously about an axis parallel to the local spacecraft vertical and measures the upwelling scene brightness temperatures. It is calibrated using cold sky radiation and a hot reference absorber. The swath is approximately 1400 km. The data are converted into sensor counts and transmitted to the National Environmental Satellite, Data, and Information Service (NESDIS). The SSM/I is an excellent sensor for measuring the brightness temperature of very large regions. For example, a SSM/I passive microwave image of almost the entire Amazon Basin is shown in Figure 9-30.

NOAA has developed a SSM/I rainfall algorithm that utilizes the 85.5 GHz channel to detect the scattering of upwelling radiation by precipitation-sized ice particles within the rain layer. The scattering technique is applicable over the land and the ocean. Rain rates can be derived indirectly, based on the relationship between the amount of ice in the rain layer and the actual rainfall on the surface. In addition, a scattering-based global land rainfall algorithm has been developed. Monthly rainfall at 100 x 100 km and 250 x 250 km grids have been produced for the period from July, 1987 to the present (Ferraro, 1997; Li et al., 1998).

TRMM Microwave Imager (TMI)

The Tropical Rainfall Measuring Mission (TRMM) is sponsored by NASA and the National Space Development Agency (NASDA) of Japan to study the tropical rainfall and the associated release of energy that helps to power global atmospheric circulation. It carries five instruments and was launched on November 27, 1997. The TRMM Microwave Imager (TMI) is a passive microwave sensor designed to provide quantitative rainfall information over a 487-mile (780 km) swath. It is based on the design of the SSM/I. It measures the intensity of radiation at five frequencies: 10.7 (45 km spatial resolution), 19.4, 21.3, 37, and 85.5 GHz (5 km spatial resolution). Dual polarization at four frequencies provides nine channels. The new 10.7 GHz frequency provides a more linear response for the high rainfall rates common in tropical rainfall.

Calculating the rainfall rates from both the SSM/I and TMI sensors requires complicated calculations because water bodies such as oceans and lakes emit only about one-half the energy specified by Planck's radiation law at microwave frequencies. Therefore, they appear to have only about half their actual temperature at the surface and appear very "cold" to a passive microwave radiometer. Fortunately, raindrops appear to have a temperature that equals their real temperature and appear "warm" or bright to a passive microwave radiometer. The more raindrops, the warmer the whole scene appears. Research over the last three decades has made it possible to obtain relatively accurate rainfall rates based on the temperature of the passive microwave scene.

Land is very different from oceans in that it emits about 90 percent of its real temperature at microwave frequencies. This reduces the contrast between the rain droplets and the land. Fortunately, the high-frequency microwaves (85.5 GHz) are strongly scattered by ice present in many raining clouds. This reduces the microwave signal of the rain at the satellite and provides a contrast with the warm land background, allowing accurate rainfall rates to be computed over land as well.

Advanced Microwave Scanning Radiometer (AMSR)

The AMSR is to be flown as an EOS PM-1 sensor in polar, Sun-synchronous orbit. It will be an eight frequency passive microwave radiometer that measures frequencies at 6.9, 10.7, 18.7, 23.8, 36.5, and 89 (HV polarization) and 50.3 and 52.8 (VV polarization). It will have a 7 km field of view at 89 GHz and 60 km field of view at 6.9 GHz. It will have a 1600 km swath width. The AMSR will measure total water-vapor content, total liquid-water content, precipitation, snow-water equivalent, soil moisture (using the 6.9 and 10.7 GHz frequencies), sea-surface temperature (SST), sea-surface wind speed, and sea-ice extent. The specifications of the sensors are subject to change.

From this discussion it should be clear that passive microwave remote sensing is making a significant contribution to our Earth science knowledge.

Light Detection and Ranging (LIDAR)

Elevation information is a critical component of most geographic databases. Several methods have been derived to measure the elevation of features, with varying degrees of accuracy and cost (Flood and Gutelius, 1997), including *in situ* field surveying, photogrammetry, SAR interferometry, and LIDAR data collection. Field surveys generally require a team of people to measure distances and angles across the landscape. Methods for such surveys are well developed and can result in very accurate information, and may include the use of GPS instruments. However, the field methods are time-consuming and expensive on a per-point basis. In rugged or heavily vegetated areas, the ground-based surveys can be difficult. Due to these obstacles, sometimes the density of x,y,z observations is not very high, making it necessary to interpolate some distance between points to produce a digital elevation model of the area.

Photogrammetric techniques are also routinely used to collect x,y,z topographic information (refer to Chapter 6). This method traditionally covers a larger area with a more dense collection of x,y,z points. In fact, Chapter 6 summarizes how digital elevation models are extracted directly from stereoscopic aerial photography. An advantage of photogrammetric techniques is that it allows the analyst to select critical features such as ridgelines or breaklines, where a greater density of x,y,z observations can be extracted. LIDAR does not allow the analyst to control the placement of individual x,y,z measurements.

LIDAR is a relatively new technology that offers an alternative to *in situ* field surveys and photogrammetric techniques for the collection of elevation data. Although technologically complex, LIDAR provides a methodology that is accurate, timely, capable of operating in difficult terrain, and increasingly affordable (Flood and Gutelius, 1997).

LIDAR Sensor System

The first optical laser was developed in 1960 by Hughes Aircraft, Inc. Soon laser-based instruments were computing distance by measuring the travel time of light from a laser transmitter to a target and then back to a laser receiver (Ritchie, 1996). Early uses of LIDAR employed a profiling laser, which only collected measurements directly underneath the aircraft, creating a single transect of measurements across the landscape (Jensen et al., 1987). Modern LIDAR systems offer several improvements over these earlier profiling systems. The integrative use of kinematic GPS and inertial navigation systems on airborne LIDAR platforms has allowed the technology to mature into commercially available systems whose price and cost of operation are generally similar to that of photogrammetric equipment used for similar purposes (Flood and Gutelius, 1997).

The essence of LIDAR technology is the measurement of laser pulse travel time from the transmitter to the target and back to the receiver. Since the laser pulse travels at the speed of light (3×10^8 m s^{-1}), very accurate timing is necessary to obtain fine vertical resolutions. A one nanosecond timing resolution, for example, allows a range measurement accuracy of about 30 cm. Timing technology allows for measurements of < 5 cm (Ritchie, 1996).

As the aircraft moves forward, a scanning mirror directs the laser pulses back and forth across-track (Figure 9-31a). The maximum off-nadir scan angle for the instrument is generally tunable to the needs of a particular data-collection mission. This results in a series of data points arranged across the flightline, as shown in Figure 9-31b. This example displays hits on bare ground, a power transmission line and tower, and the effects of the laser interacting with a tree canopy. Multiple flightlines can be combined to cover the desired area. Data-point density is dependent on the number of pulses transmitted per unit time, the scan angle of the instrument (Figure 9-31c), the elevation of the aircraft above-ground-level, and the forward speed of the aircraft. Note that the greater the scan angle off-nadir, the more vegetation that will have to be penetrated to receive a pulse from the ground assuming a uniform canopy.

LIDAR data avoids the problems of aerial triangulation and orthorectification because each LIDAR measurement is individually georeferenced (Flood and Gutelius, 1997). This requires measurement of several important factors, including:

- the laser pulse travel time from the LIDAR instrument to the target (ground) and back,
- the scan angle of the LIDAR at the time of the laser pulse,
- the effect of atmospheric refraction on the speed of light,
- the attitude (pitch, roll, and heading) of the aircraft at the time of the laser pulse, and
- the position of the LIDAR instrument in three-dimensional space at the time of the laser pulse.

The LIDAR records the scan angle of the mirror and the travel time of the laser pulse to and from the target. Atmospheric refraction has a slight effect on the speed of light that should be taken into account in the conversion from laser pulse travel time to distance. Aircraft attitude is recorded by an inertial navigation unit that takes careful measurements of the aircraft's pitch, roll, and heading. Combined with the information recorded from the scanning mirror, the attitude measurements allow precise determination of where the LIDAR instrument was pointed at the time of an individual laser pulse. Aircraft position is determined from GPS equipment located on the aircraft.

During the LIDAR overflight, one or more GPS base stations must be recording positional data on the ground in the area of the overflight. These base stations are located at known points, and the data they collect is used to remove any GPS error resulting from atmospheric effects and selective availability. This differential correction allows the aircraft location to be known within 5 – 10 cm accuracy in all three axes (Vaughn et al., 1996).

The combination of all these factors allows three-dimensional georeferenced coordinates to be determined for each laser pulse. There are several other factors and calibrations required for accurate LIDAR georeferencing, including timing accuracy, range dispersion within the laser footprint, "range walk" due to backscatter strength variations, and syn-

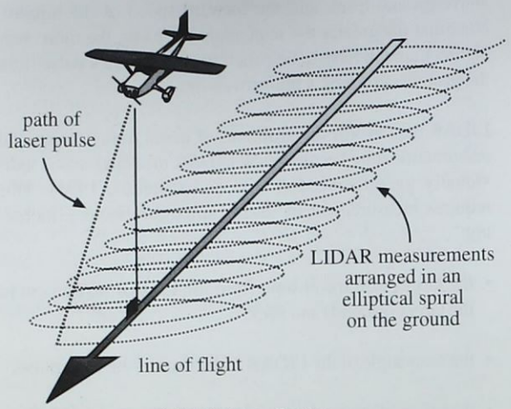

a. LIDAR data collection.

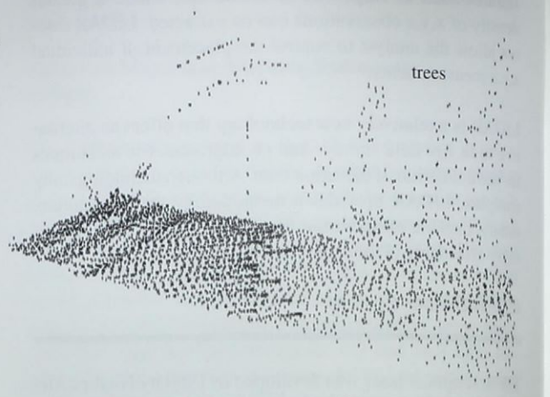

b. Actual LIDAR hits for a small area.

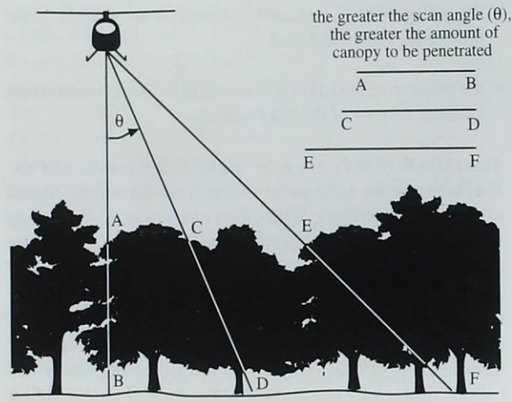

c. Impact of increased scan angle.

d. LIDAR derived digital elevation model.

Figure 9-31 a) Logic of LIDAR data collection showing the line of flight and the elliptical spiral of points that are backscattered from the terrain as the aircraft moves forward. b) LIDAR-derived location (x,y) and elevation (z) data for a small portion of the study area. The LIDAR does well on the unvegetated left portion of the area. It is so sensitive that it even hits the power transmission line in the center. It begins to interact with the tree canopy on the right. c) Assuming that the tree canopy has a uniform height and canopy density, then the greater the scan angle from nadir the greater the amount of canopy that will have to be penetrated to reach the ground to acquire the information necessary to create a digital elevation model. d) A reduced image of a LIDAR-derived digital elevation model for an area near Aiken, SC.

chronization errors among the data streams (Vaughn et al., 1996; Ridgway et al., 1997; Krabill et al., 1995).

Accuracy of LIDAR Measurements

Using test flights over Lake Crowley, CA, Vaughn et al. (1996) reported vertical accuracies within ± 2-13 cm of a local USGS tide gauge with a mean error of ± 6 cm. Another project at Lake Crowley found the absolute height difference to be 1 – 4 cm (Ridgway et al., 1997). During their work on the Greenland ice sheet, Krabill et al. (1995) used a runway for testing the instrument's accuracy from the air and found the measurements to be accurate within approximately ± 10 cm of the runway's surveyed elevation. Recent research indicates that LIDAR can provide measurements with vertical accuracy of less than 10 cm. Vaughn et al. (1996) believe that if care is taken in the numerous calibrations and corrections, then consistent accuracies of ± 5 cm can be obtained.

Canopy Penetration Capability

One of the unique properties of LIDAR is the ability to penetrate vegetation canopy and to map the surface below. Although some of the laser energy will be backscattered by vegetation above the ground surface, only a portion of the laser needs to reach the ground to produce a surface measurement. Both of these partial returns (vegetation and ground) can be recorded by the LIDAR instrument, allowing measurements of both vegetation canopy height and ground-surface elevation. Some LIDAR instruments are capable of recording up to five laser returns from a single pulse. Figure 9-31b shows a section of LIDAR data where both ground measurements and canopy measurements were obtained.

The ability to see both vegetation and the ground surface has useful applications in measuring vegetation attributes. Nilsson (1996) examined the usefulness of LIDAR for estimating timber volume as a part of Sweden's National Forest Inventory. Weltz et al. (1994) used a profiling LIDAR system to map vegetation height and canopy cover at the Walnut Gulch experimental watershed in Arizona. This study demonstrated the ability of LIDAR to distinguish between different vegetation communities and ground-cover types. Nelson et al. (1988) successfully used LIDAR to estimate forest biomass and volume to within 2.6 percent and 2.0 percent, respectively, on 38 test plots in southwestern Georgia.

If the purpose of a LIDAR overflight is to collect data for creating digital elevation models (DEMs), the presence of vegetation can be a nuisance. In areas covered by dense vegetation, the majority of the LIDAR measurements will be in the canopy, with only a few reaching the ground. Hendrix (1999) found that up to 93% of LIDAR pulses never reached the ground in mixed bottomland hardwoods near Aiken, SC. Separating the ground measurements from measurements of vegetation, buildings, and other structures can be difficult, especially if only a few measurements of the ground are made through the canopy. A single LIDAR overflight can produce millions of measurements, and current research is seeking to identify the best methods for automated identification and extraction of ground measurements.

References

Aero Service Corp., 1978, *SAR Synthetic Aperture Radar*, Houston, TX: Aero Service Corporation, 14 pp.

Avery, T. E. and G. L. Berlin, 1992, *Fundamentals of Remote Sensing and Airphoto Interpretation*, 5th Ed., Upper Saddle River: Prentice-Hall, Inc., 472 pp.

Blom, R. G., L. R. Schenck and R. E. Alley, 1987, "What are the Best Radar Wavelengths, Incident Angles, and Polarizations for Discrimination Among Lava Flows and Sedimentary Rocks? A Statistical Analysis," *IEEE Transactions on Geoscience and Remote Sensing*, GE-25(2):209–212.

Campbell, J. B.,1996, *Introduction to Remote Sensing*. New York: The Guilford Press.

Carver, K. R., 1988, SAR *Synthetic Aperture Radar – Earth Observing System*, Vol. IIf, Washington: NASA Instrument Panel Report, 233 pp.

Carver, K. R., E. Elachi and F. T. Ulaby, 1985, "Microwave Remote Sensing from Space," *Proceedings of the IEEE*, 7(6):970–996.

Committee on Earth Sciences, 1990, *Our Changing Planet: The FY 1991 Research Plan - U.S. Global Change Research Program.* Washington: Federal Coordinating Council for Science, Engineering, & Technology, 60 pp.

Curran, R. J., 1989, "NASA's Plans to Observe the Earth's Atmosphere with LIDAR," *IEEE Transactions on Geoscience and Remote Sensing*, 27:154–163.

Dobson, M. C. and F. T. Ulaby, 1998, "Mapping Soil Moisture Distribution with Imaging Radar," Lewis and Henderson (Eds.), *Principles and Applications of Imaging Radar*, New York: John Wiley & Sons, 407–433.

Dobson, M. C., F. T. Ulaby, T. LeToan, A. Beaudoin, E. S. Kasischke and N. Christensen, 1992, "Dependence of Radar Backscatter on Coniferous Forest Biomass," *IEEE Transactions on Geoscience and Remote Sensing*, 30(2):412–415.

Dobson, M. C., F. T. Ulaby, L. E. Pierce, T. L. Sharik, K. M. Bergen, J. Kellndorfer, J. R. Kendra, E. Li and Y. C. Lin, 1995, "Estimation of Forest Biomass Characteristics in Northern Michigan with SIR-C/S-SAR Data," *IEEE Trans. Geosci. Remote Sensing*, 33:877–894.

Elachi, C., et al. 1982, "Shuttle Imaging Radar Experiment," *Science*, 218, 996–1004.